REPORT DOCUMENTATION PAGE

AFRL-SR-BL-TR-00-

0719

1. AGENCY USE ONLY *(Leave blank)*	2. REPORT DATE	3. REPORT TYPE AND DATES COVERED
	11/1/2000	Final Report

4. TITLE AND SUBTITLE
Synthetic Aperture Radar Signal Processing and Imaging Using High Performance Computing

5. FUNDING NUMBERS
F49620-99-1-0140

6. AUTHOR(S)
Mehrdad Soumekh

7. PERFORMING ORGANIZATION NAMES(S) AND ADDRESS(ES)
Department of Electrical Engineering
State University of New York at Buffalo
332 Bonner Hall
Buffalo, NY 14260

8. PERFORMING ORGANIZATION REPORT NUMBER

9. SPONSORING / MONITORING AGENCY NAMES(S) AND ADDRESS(ES)
AFOSR/NM
801 N. Randolph Street
Arlington, VA 22203-1977

10. SPONSORING / MONITORING AGENCY REPORT NUMBER

11. SUPPLEMENTARY NOTES

a. DISTRIBUTION / AVAILABILITY STATEMENT
Approved for public release.

12. DISTRIBUTION CODE

13. ABSTRACT *(Maximum 200 words)*

The grant was provided by AFOSR to establish a SAR High Performance Laboratory. With this support, the following items were purchased for the SAR HPC laboratory: 16 Origin-2000 300 MHz Processors; 8 GBytes of RAM; 108 GBytes of Fiber Channel Hard Drive; OCTANE Workstation with a 300 MHz RS-12000 Processor, and Enhanced SSE Graphics. During the past two summers, the PI also collaborated with the members of the Air Force's Rome Laboratory (Contact: Mark Linderman) and Wright Patterson Laboratory (Steve Worrell, Ed Zelnio and Mike Bryant) on various implementation aspects of SAR signal and image processing algorithms on Shared Memory Processors (SMP) and Distributed Memory (DM) HPCs. The results of these collaborations are documented in the attached three papers.

14. SUBJECT TERMS	15. NUMBER OF PAGES
SAR, HPC	35
	16. PRICE CODE

17. SECURITY CLASSIFICATION OF REPORT	18. SECURITY CLASSIFICATION OF THIS PAGE	19. SECURITY CLASSIFICATION OF ABSTRACT	20. LIMITATION OF ABSTRACT
Unclassified	Unclassified	Unclassified	

Final Report for:

CONTRACT F49620-99-1-0140 (DURIP 99)

SYNTHETIC APERTURE RADAR SIGNAL PROCESSING AND IMAGING USING HIGH PERFORMANCE COMPUTING

Submitted to:

Dr. Jon A. Sjogren or Mark Gruneisen, Scientific Officer
AFOSR/NM
801 N. Randolph Street
Arlington, VA 22203-1977

ONRRO Boston
495 Summer Street, Rm 103
Boston, MA 02210-2109

Defense Technical Information Center
8725 John J. Kingman Road
STE 0944
Ft. Belvoir, VA 22060-6218

Distribution Statement:

Approved for public release.

Project Director:

Mehrdad Soumekh
Department of Electrical Engineering
State University of New York at Buffalo
Amherst, New York 14260
Phone: (716) 645-2422, extension 2138
Fax: (716) 645-3656
Email: msoum@eng.buffalo.edu

Final Report:

Synthetic Aperture Radar Signal Processing and Imaging Using High Performance Computing

Mehrdad Soumekh
Department of Electrical Engineering
State University of New York at Buffalo
Amherst, New York 14260

This document describes the progress on the work performed for "Synthetic Aperture Radar Signal Processing and Imaging Using High Performance Computing," under the DURIP Contract F49620-99-1-0140 for the Air Force Office of Scientific Research, for the period ending on 9/30/2000.

The grant was provided by AFOSR to establish a SAR High Performance Laboratory. With this support, the following items were purchased for the SAR HPC laboratory:

1. 16 Origin-2000 300 MHz Processors
2. 8 GBytes of RAM
3. 108 GBytes of Fiber Channel Hard Drive
4. OCTANE Workstation with a 300 MHz RS-12000 Processor, and Enhanced SSE Graphics

During the past two summers, the PI also collaborated with the members of the Air Force's Rome Laboratory (Contact: Mark Linderman) and Wright Patterson Laboratory (Steve Worrell, Ed Zelnio and Mike Bryant) on various implementation aspects of SAR signal and image processing algorithms on Shared Memory Processors (SMP) and Distributed Memory (DM) HPCs.

During the first part of the summer of 1999, the PI worked with the group at the Rome Lab. to work on the parallel implementation of his SAR imaging algorithms on HPCs. A subaperture digital spotlight SAR imaging method was developed that was suitable for implementation in both SMP and DM HPCs. The algorithm was tested using a wide-bandwidth and wide-beamwidth FOPEN SAR (P-3) database.

During the second part of the summer of 1999 and summer of 2000, the PI worked with the group at the Wright Pattern Lab. to implement his high-resolution SAR imaging (wavefront reconstruction) algorithms on realistic X band spotlight SAR databases. The subaperture digital spotlight SAR imaging method was successfully implemented for an operational wide angle spotlight SAR system.

The results of these collaborations are documented in the attached three papers.

Digitally-Spotlighted Subaperture SAR Image Formation Using High Performance Computing

Mehrdad Soumekh and Gernot Günther
Department of Electrical Engineering, 201 Bell Hall
State University of New York at Buffalo
Amherst, New York 14260
Email: msoum@eng.buffalo.edu

Mark Linderman and Ralph Kohler
United States Air Force Research Laboratory
Radar Signal Processing Branch
Rome, NY 13441

ABSTRACT

This paper is concerned with the implementation of the SAR wavefront reconstruction algorithm on a high performance computer. For this purpose, the imaging algorithm is reformulated as a coherent processing (spectral combination) of images that are formed from a set of subapertures of the available synthetic aperture. This is achieved in conjunction with extracting the signature of a specific target region (digital spotlighting). Issues that are associated with implementing the algorithm on SMP-HPCs and DMP-HPCs are discussed. The results using the FOPEN P-3 SAR data are provided.

Keywords: Synthetc Aperture Radar. High Performance Computing

1. INTRODUCTION

This paper presents a practical method for implementing the high-resolution stripmap/spotlight SAR imaging algorithm, known as the SAR wavefront (or omega-k) reconstruction method, on a Distributed Memory (DM) High Performance Computer (HPC). The SAR wavefront imaging method is an approximation-free algorithm that provides high-resolution and accurate coherent target information that is useful for advanced SAR information post-processing, e.g., automatic target recognition. However, the highly-accurate information base of the wavefront reconstruction algorithm is formed via the Fourier (FFT) processing of relatively large databases. For real-time processing in an operational SAR system, this requirement puts restrictions on the minimum size of the Random Access Memory (RAM) of the computer used for the SAR wavefront image formation.

Meanwhile, due to the limited area and cooling restrictions on a radar-carrying aircraft, the DM-HPCs are the practical choice for on board processing of SAR data. Unfortunately, in a DM-HPC, unlike a shared memory HPC, the RAM associated with each processor cannot be addressed by the other processors. In this case, the RAM available to each DM processor (currently around 64 to 128 MBytes) is not sufficient for, e.g, processing some of the recently-acquired high-resolution X band or UHF band (FOPEN) SAR data via the wavefront reconstruction algorithm. A practical solution for the above-mentioned problem is to form lower-resolution images of subpatches of the target area from subsets of the synthetic aperture or synthetic *subapertures*; this reduces the sizes of the data that are processed and the FFTs used for the wavefront reconstruction. Moreover, the sizes of the subpatch and subapertures can be determined a priori

The work of Mehrdad Soumekh was supported by the Office of Naval Research under grants N00014-96-1-0586 and N00014-97-1-0966, and the Air Force Office Of Scientific Research under grants F49620-99-1-0140 and F49620-93-C-0063.

by the user based on the available RAM. Provided that the subaperture imaging algorithm preserves the coherent information among the lower-resolution images, the user could coherently add the lower-resolution images to form the desired high-resolution SAR image.

The challenge for this processing is i) to extract the SAR signature of a given subpatch from the measured SAR data, a process that we refer to as *digital-spotlighting;* and ii) appropriate digital signal processing of subaperture SAR data that yields "calibrated" lower-resolution SAR images that can be combined coherently. In this presentation, we address these issues via exploiting spectral (Doppler) properties of the SAR signal that is based on Gabor's wavefront reconstruction theory. In Section 2, we outline subaperture digital spotlighting and reconstruction for stripmap/spotlight SAR systems. In Section 3, we show how the lower-resolution SAR images that are formed with subaperture data could be coherently combined to form the full-resolution image. This discussion also shows that subaperture processing is more advantageous in terms of the size of the arrays that are processed than the full-aperture processing: results using a realistic stripmap SAR database (P-3 data) will be provided. Finally, we examine issues that are associated with the implementation of the imaging algorithm on a high performance computer in Section 4, and present the results of a study that we performed with an HPC.

2. Subaperture Digital Spotlighting

We consider the problem of imaging a specific target area in the two-dimensional spatial domain of range x and cross-range y from a subset of a synthetic aperture (subaperture) within which the target area is *observable* to the radar; the synthetic aperture could be a portion of a full aperture of a spotlight SAR system, or a subset of the beamwidth (subaperture) in a stripmap SAR system that contains the desired target area.

Suppose the length of the subaperture is $2L$; that is. $u \in [-L, L]$, where u is the synthetic aperture domain. Let the coordinates of the center point of the target area with respect to the center point of the subaperture (that is, $u = 0$) be (X_c, Y_c). The user is interested in imaging an area in the spatial domain that is specified via

$$x \in [X_c - X_0, X_c + X_0] \quad \text{and} \quad y \in [Y_c - Y_0, Y_c + Y_0],$$

with respect to the center of the subaperture, that is, $u = 0$. Our task is to develop a multi-dimensional digital signal processing method to *extract* the SAR signature of the above-mentioned target area from the spotlight/stripmap measurements, a process that we refer to as *digital spotlighting.*

Let $s(\omega, u)$ be the measured SAR signal in the fast-time frequency ω domain and the synthetic aperture u domain. To formulate the digital spotlighting concept. consider the target function which is formed via narrow-bandwidth and narrow-beamwidth polar format processing at near broadside [S99, Section 4.11]; that is,

$$F(k_x, k_y) = s_c(\omega, u),$$

where

$$k_x = 2k \cos\theta_c \quad \text{and} \quad k_y = 2k_c \sin\theta_c - 2k_c \frac{\cos^2\theta_c}{R_c} u.$$

In the above, $R_c = \sqrt{X_c^2 + Y_c^2}$ and $\theta_c = \arctan\left(\frac{Y_c}{X_c}\right)$, and

$$s_c(\omega, u) = s(\omega, u) \exp\left[\sqrt{X_c^2 - (Y_c - u)^2}\right],$$

is the *slow-time compressed* SAR signal. In this case. the target function $f(x, y)$ is simply the two-dimensional Fourier transform of the slow-time compressed signal, that is, the slow-time compressed SAR signal in the (t, k_u) domain.

In [S99, Section 4.11], it is pointed out that a more accurate analysis of the SAR image which is formed via polar format processing would indicate that the signature of the n-th target. that is located at the spatial rectilinear coordinates (x_n, y_n) or the the polar spatial coordinates $[\theta_n(0), r_n]$, appears at

$$t_n \approx \frac{2r_n}{c} \quad \text{and} \quad k_{un} \approx 2k_c \sin\left[\theta_n(0) - \theta_c\right]$$

in the polar format processed SAR image, that is, the two-dimensional Fourier transform $\mathcal{F}_{(\omega,u)}\Big[\, s_c(\omega, u)\,\Big]$, which we refer to as the polar format processed reconstruction. (The Fourier transform with respect to the variable ω is an inverse one.)

Note that the above transformation from (r_n, θ_n) to (t_n, k_{un}) can be translated into the following rectilinear coordinates in the spatial domain:

$$x_n = \frac{c\, t_n}{2} \cos(\phi_n + \theta_c) \quad \text{and} \quad y_n = \frac{c\, t_n}{2} \sin(\phi_n + \theta_c)$$

where $\phi_n = \arcsin\left(\frac{k_{un}}{2k_c}\right)$. Thus, for digital spotlighting the desired target area, that is, $x \in [X_c - X_0, X_c + X_0]$ and $y \in [Y_c - Y_0, Y_c + Y_0]$, the polar format processed image in the (t, k_u) domain should be passed through a two-dimensional filter in the (t, k_u) domain with the following passband:

$$\left|\frac{c\, t}{2} \cos(\phi + \theta_c) - X_c\right| < X_0 \quad \text{and} \quad \left|\frac{c\, t}{2} \sin(\phi + \theta_c) - Y_c\right| < Y_0$$

where $\phi = \arcsin\left(\frac{k_u}{2k_c}\right)$ is the *angular* slow-time Doppler domain at the carrier frequency [S99. Chapter 2].

We should point out that this definition of the angular slow-time Doppler ϕ domain is suitable for the *narrow-bandwidth* SAR systems. One could improve the results of digital spotlight filtering by converting the SAR signal $S_c(\omega, k_u)$ into the (ω, ϕ) domain where $\phi = \arcsin\left(\frac{k_u}{2k}\right)$ is the angular slow-time Doppler domain which varies with the fast-time frequency. For this purpose, at a fixed ω or k, one must interpolate $S_c(\omega, k_u)$ from the k_u domain to the ϕ domain. Then, this database is converted into the (t, o) domain via an inverse Fourier transform with respect to ω. The digital spotlight window is then applied to this (t, ϕ) domain database. The digital-spotlighted data are then brought back to the (ω, ϕ) domain via a forward Fourier transform with respect to t. The resultant (ω, ϕ) domain data are interpolated to recover the (ω, k_u) domain data via the wide-bandwidth mapping $\phi = \arcsin\left(\frac{k_u}{2k}\right)$, or $k_u = 2k \sin\phi$.

Thus, for the wide-bandwidth SAR systems, one needs to implement one-dimensional interpolation from the k_u domain to the ϕ domain, and then back from the ϕ domain to the k_u domain. It turns out that using the narrow-bandwidth assumption, that is, $\phi = \arcsin\left(\frac{k_u}{2k_c}\right)$, for digital spotlighting results in slight degradations near the edges of the reconstructed SAR image; these are negligible effects especially when the purpose is to image a large target area. (One may reduce and/or completely remove these degradations by using a larger digital spotlight filter.) In the discussion and the results which follow, we use the narrow-bandwidth assumption for digital spotlighting.

The procedure for digital spotlighting can be summarized as follows. The reference SAR signal is defined via

$$s_0(u, \omega) = \exp\left[-j2k \sqrt{X_c^2 + (Y_c - u)^2} + j2k\, R_c\right];$$

the addition of the phase term $2k\, R_c$ to the reference signal ensures that the reference fast-time point T_c is unchanged. The digital spotlight filter in the (t, k_u) domain is defined via

$$W_d(t, k_u) = \begin{cases} 1, & \text{for } \left|\frac{c\, t}{2} \cos(\phi + \theta_c) - X_c\right| < X_0 \text{ and } \left|\frac{c\, t}{2} \sin(\phi + \theta_c) - Y_c\right| < Y_0; \\ 0, & \text{otherwise.} \end{cases}$$

Polar format processed reconstruction with the digital spotlight filter is

$$f_d(t,k_u) = W_d(t,k_u)\ \mathcal{F}_{(\omega,u)}\Big[\ s_c(\omega,u)\ \Big].$$

Then, the digital-spotlighted slow-time compressed SAR signal in the (ω,k_u) domain is obtained by

$$S_{cd}(\omega,k_u) = \mathcal{F}_{(t)}\Big[\ f_d(t,k_u)\ \Big].$$

At this point, if the user wishes to upsample the SAR data in the synthetic aperture u domain (that is, sample spacing conversion from Δ_{uc} to Δ_u), an appropriate number of zeros should be added to the samples of $S_{cd}(\omega,k_u)$ in the slow-time Doppler k_u domain [S99, Chapter 2]. After the optional zero-padding in the k_u domain, the digital-spotlighted slow-time compressed signal in the (ω,u) domain is formed via

$$s_{cd}(\omega,u) = \mathcal{F}^{(-1)}_{(k_u)}\Big[\ S_{cd}(\omega,k_u)\ \Big].$$

Finally, the digital-spotlighted SAR signal in the (ω,u) domain is constructed from the following slow-time decompression (mixing with the reference SAR signal): $s_d(\omega,u) = s_{cd}(\omega,u)\ s_0(u,\omega)$.

In this paper, we examine the processing of UHF-band P-3 (FOPEN) SAR data. Figure 1a shows the reconstructed target spectrum for 2,048 slow-time samples of P-3 data for a 300 m (in range) and 600 m (in cross-range), that is, $(X_0,Y_0) = (150,300)$ m, which is located at $(X_c,Y_c) = (5857.-2048)$ m: the spatial domain image formed by this spectrum is shown in Figure 1b. Note that the individual "dots" (two-dimensional sinusoids) in the reconstructed target spectrum of Figure 1a; these are the signatures of RFI's (mainly audio and video channels of various television stations). We used a process to convert the deramped P-3 data into echoed data [S99]. This approach makes the RFI signatures to appear as individual dots that are easier to suppress. (In the spatial reconstruction of Figure 1b, the RFI signatures are not suppressed to exhibit the *sinusoidal* behavior of them.) We also obtain the lower-resolution reconstructions of the target area for the subapertures with squint cross-range values of Y_c = -1228.8 m, -409.6 m, 409.6 m, 1228.8 m, and 2048 m (each subaperture has 2,048 slow-time samples); these are not shown in this paper.

3. Coherent Subaperture Digital Spotlighting

The reconstructed target function in Figure 1b is formed via processing a subset of the aspect angle (slow-time) domain data over which the target area is observable to the radar. Since the wavefront reconstruction is not based on any approximations (on the relative size and/or coordinates of the target area with respect to each individual subaperture), one can combine these lower-resolution images (and their three positive squint angle counterparts) to obtain the full-resolution SAR image of the target area.

For this purpose, one could combine the target area's spectral signature that appears in Figure 1a and its five other counterparts (i.e., six spectral bands formed by six different subapertures), and then perform an inverse two-dimensional Fourier transform to form the full-resolution spatial domain SAR image. Figure 2 shows the combined spectral distribution of the target area from its six subaperture spectra.

Note that the slow-time Doppler bands (that is, the k_y domain coverage) for the subaperture reconstructions (e.g., Figure 1a) are smaller than the full-aperture reconstruction Doppler band in Figure 2. In fact, the sizes of the *processed* measurement arrays and the FFTs that are used to form the lower resolution subaperture images are significantly smaller than the ones used for the full-aperture reconstruction. To show this, we consider the Nyquist sampling rate for the slow-time domain which is the smallest of [S99]

$$\Delta_u \le \frac{\lambda_{\min}}{2\ (\sin\theta_{\max} - \theta_{\min})} \quad \text{and} \quad \Delta_u \le \left[\ \frac{2\sin\theta_{\max}}{\lambda_{\min}} - \frac{2\sin\theta_{\min}}{\lambda_{\max}}\ \right]^{-1},$$

where $\lambda_{\min}$ and $\lambda_{\max}$ are, respectively, the smallest and largest wavelengths in the radar signal. and

$$\theta_{\min} = \arctan\left(\frac{Y_c - L - Y_0}{X_c}\right) \quad \text{and} \quad \theta_{\max} = \arctan\left(\frac{Y_c + L + Y_0}{X_c}\right)$$

are the smallest and largest aspect angles of the target area (a positive Y_c is assumed. and some simplifications are used to relax our notation; for the complete story, see [S99]).

In the case of the P-3 data, there are 12,288 (six times 2,048 samples) slow-time samples spaced at $\Delta_u = .4$ m. Thus, to form the full-resolution SAR image by processing the entire 12,288 slow-time samples, the slow-time Nyquist criterion becomes $\Delta_u \leq .22$ m; that is, the slow-time domain data should be upsampled to over 22,000 samples (see the discussion on PRF upsampling via the slow-time compression in [S99]). However, for the subaperture reconstruction, the slow-time Nyquist criterion is $\Delta_u \leq .92$ m for $Y_c = \pm 409.6$ m; $\Delta_u \leq .66$ m for $Y_c = \pm 1228.8$ m; and $\Delta_u \leq .52$ m for $Y_c = \pm 2048$ m; In this case, there is no need to upsample in the slow-time domain. Iin fact, in our processing, we reduce the sampling rate in the slow-time domain (depending on the value of Y_c) since the measured P-3 data is with $\Delta_u = .4$ m.

4. Implementation on a High Performance Computer

We have developed the subaperture digital-spotlighting and coherent imaging algorithm using a Matlab code. This code has been successfully being used to process the following five different SAR/ISAR databases:

i. NRaD's X-band ISAR data
ii. SRI's UHF-band (FOPEN) SAR data
iii. NAVAIR/ERIM's UHF-band (P-3 FOPEN) SAR data
iv. ERIM's X-band DDB SAR data
v. ERIM's Ultra-SAR data

This Matlab code has been converted to an efficient C code that is suitable for implementation on an HPC. The following is a summary of the outcomes and observations in using this C code to process P-3 data on a 16-processor 8-GBytes-RAM SGI SMP-HPC. To improve the performance of the code from the computational cost point of view, we first considered its sequential optimization; we then studied its parallel implementation. These are described next.

A. Sequential Optimizations

Fourier Transforms: Processing SAR data requires numerous one-dimensional and two-dimensional Fourier transforms. Thus, it was important to utilize a fast Fourier transform code in C. A great deal of research has been done on this subject. We chose to use the fftw library [Fri]. This library determines the optimal decomposition of a Fourier transform on the system in use by performing a number of sample Fourier transforms, and is easily parallelizable. However, fftw does not automatically choose the fastest way of implementing a transform: The user still has to test whether it is more efficient to implement a non-contiguous transform or a transposition and a contiguous transform, and how many threads to use for a parallel FFT. These choices depend greatly on the size of the data used and will also differ from system to system. There are some general rules to follow, but no automated functions that will aid in these choices. Also, this library does not implement an integrated FFT-shift operation, so from case to case, decisions had to be made on how best to integrate or avoid this operation. The array sizes of the SAR data were adjusted to allow particularly fast Fourier transforms where possible.

Combining Operations: The main focus in the process of sequential optimization lies in the simplification of the computation and in reduction of redundancy. A clear indication that a code is not optimized yet is when the program spends a lot of its time merely copying data. Very often, this can be completely avoided by forcing in-place calculations. Operations that inherently involve copying, like FFT-shift or zero-padding, can sometimes be combined with each other and with other calculations and thereby reduce the copying significantly. Another good example of a reducible operation is performing several phase shifts in one step, e.g., chirp signal calibration and motion compensation. This will significantly improve the speed of the code and is trivial from a mathematical point of view. Unfortunately, it also reduces the readability of the code because operations are combined that are considered separate from a radar imaging point of view. In a code that is optimized in this way, it may be rather difficult to track the different parts of each processing step as they may be integrated into different modules.

B. Parallel implementation

Two very different ways of parallelization have to be considered: Parallelism can occur at the lowest level, e.g., by using a parallel Fourier transform, or at the highest level by running the optimized sequential algorithm in parallel for different subapertures or targets areas. Both of these concepts have advantages and disadvantages. Running several independent sequential algorithms in parallel is very straightforward, easily implemented with a script, and keeps all available processors busy. However, the resources are not optimally used: No use is made of the SMP architecture because each process works on its own memory. A small part of the computation performed by the sequential processes is redundant and could be avoided if the processes shared their results. No single process can use the large amount of RAM available in a SMP-HPC, each of the p processes can only use an average of $1/p$ of the RAM.

Low level parallelism on the other hand requires a great amount of programming because every single part of the program has to be separately converted from sequential to parallel execution. The resulting parallel program using p processors will not be p times faster than the sequential algorithm: Creating and synchronizing threads involves a significant overhead, and not all parts of the program lend themselves equally well to parallelization. Also, the optimal sequential algorithm may not be the best algorithm to parallelize. Other problems that turn up are specific to the target architecture: A single processor working on data in its cache may finish its calculation faster than several processors working on the same data and mutually invalidating their cache entries. Because of these difficulties in low-level parallelization, we decided to primarily use high level parallelization of a single threaded process for imaging of large target areas at high resolution. However, for imaging a specific target area from a specific point of view, low-level parallelization is preferable.

C. Evaluation

As described in Section 3, it is possible to generate full resolution images from lower resolution images derived from subaperture processing. We therefore have to examine two parts of the process: Generating the subaperture spectral images and combining these images to a full resolution spatial image. The parameters of our problem are the target (sub-)area size and the size of the subapertures. The target area's dimensions in range and cross-range are $2X_0$ and $2Y_0$. The given P3 database supports values for X_0 up to 350m. It contains 24 nodes with 512 slow-time samples each. We measured the CPU time and memory requirements of the sequential algorithm for different target area sizes of a broadside target and different numbers of nodes in the subapertures. Our values for X_0 were 50, 100, 200, 300, and 350 meters. Our values for Y_0 were 100, 200, 300, 450. and 600 meters. We used subapertures containing 1, 2, 3, 4, and 6 nodes.

Figures 3a-3b show the CPU time per target area used to image that area. Figure 3a shows the results for subaperture imaging: It clearly shows that the timing efficiency increases with target area size. Figure 3b shows the result for combining the spectral images: In general, slightly better timing results are achieved for smaller target area sizes because of the 2D Fourier Transform converting the added spectral images to the spatial domain. This slight difference however is negligible in comparison to the wide range of timing results for a given target area depending on subaperture size. These timing results are so scattered because different subaperture sizes cause aperture zero-padding or Doppler subsampling in the subaperture processing, leading to different array sizes to be processed during the coherent subaperture combining. Figure 3c shows the sum of the first two figures: The CPU time per target area for creating all spectral subaperture images and combining them. Clearly, generating the lower resolution subaperture images requires much more CPU time than combining them to a full resolution image. The influence of combining the subaperture images on the total timing is negligible.

The following table shows the top ten timing results, the parameters used and the memory required for each of the two stages.

Total CPU Time / Area (msec/m^2)	X_0 (m)	Y_0 (m)	number of nodes	Average memory per subaperture (M-Bytes)	Total memory for combination (M-Bytes)
0.599154	350	600	6	963	1127
0.671711	350	600	4	656	1141
0.722609	300	600	3	505	988
0.726007	350	450	3	**471**	839
0.727505	350	600	3	560	1147
0.732468	300	600	6	915	969
0.732560	350	450	4	622	838
0.748727	300	600	4	613	982
0.764735	300	450	3	431	706
0.774671	350	450	6	955	909

Creating sub-aperture spectral images is complex, and low-level parallelization would be very difficult to implement. Therefore we want to use high-level parallelization for this task, i.e. we want to run 16 of these sequential processes at the same time, one on each processor. Since we are limited to 8 GB of RAM on our given system, some of which is needed for the operating system, we do not want to use more than an average of 500 MB of RAM for each process.

According to the table, $X_0 = 350$m, $Y_0 = 450$m, and $nodes = 3$ yields the best timing result complying with this memory limitation. Notice however that the performance could be over 17% better if our system had enough memory to support the first solution, and even slightly better results could be achieved for larger target areas if there were more memory available for each process. This performance would correspond to the best performance we could expect if this part were optimally low-level parallelized, allowing one process to use the entire available memory.

The combination of the subaperture spectral images however is very straightforward, containing only matrix additions and a 2D Fourier Transform. It is therefore easy to implement a low-level parallelization for this task. We use all available processors and are therefore not limited to a fraction of the available main memory.

D. Performance on a DMP-HCP

The implementation using high-level parallelism for the subaperture imaging does not make use of the memory-sharing capability of the SMP-HPC other than in passing the results to the coherent subaperture combining. This kind of independent parallel execution of the algorithm could just as easily be implemented on a DMP-HPC. Notice that instead of examining the average memory usage, we have to consider the maximum memory usage on a DMP-HPC.

The current DMP-HPCs used on radar carrying aircraft have only 64 MB of RAM per processor. This limits the maximum memory that a process may use for subaperture imaging. From our tests, the best results under these limitations are achieved using $X_0 = 50\text{m}$, $Y_0 = 200\text{m}$, and $nodes = 1$, yielding a total CPU time per area of 0.003081sec/m^2. This is about 4.2 times less efficient than the implementation on our SMP-HPC, therefore a DMP-HPC must have 4.2 times as many comparable processors in order to process the data in the same time.

DMP-HPCs using 128 MB of RAM per processor could process a target area corresponding to $X_0 = 200\text{m}$ and $Y_0 = 200\text{m}$ with one node per subaperture, yielding a total CPU time per area of 0.001851sec/m^2. This is 1.66 times more efficient than the implementation restricted to 64 MB of RAM. In the first scenario, the coherent subaperture combination requires only 48 MB, it could therefore run on a single processor. In the second case, 188 MB of RAM are needed. However, the memory requirements for the coherent subaperture combination do not restrict the processing parameters because the process and its memory requirements can be distributed among several processors with some loss of efficiency.

Note that the most efficient choice of X_0, Y_0, and *nodes* is not necessarily the fastest: If the set of input data or the target area of interest is small, choosing the most efficient parameters will occupy only a small number of processors. It would then be less efficient but faster to split the problem into smaller pieces so that no processors will be idle.

References

[Fri] M. Frigo and S. Johnson, "An Adaptive Software Architecture for the FFT", *Proc. ICASSP '98*, vol. 3, p. 1381.

[S99] M. Soumekh, *Synthetic Aperture Radar Signal Processing with MATLAB Algorithms*, New York: Wiley, 1999.

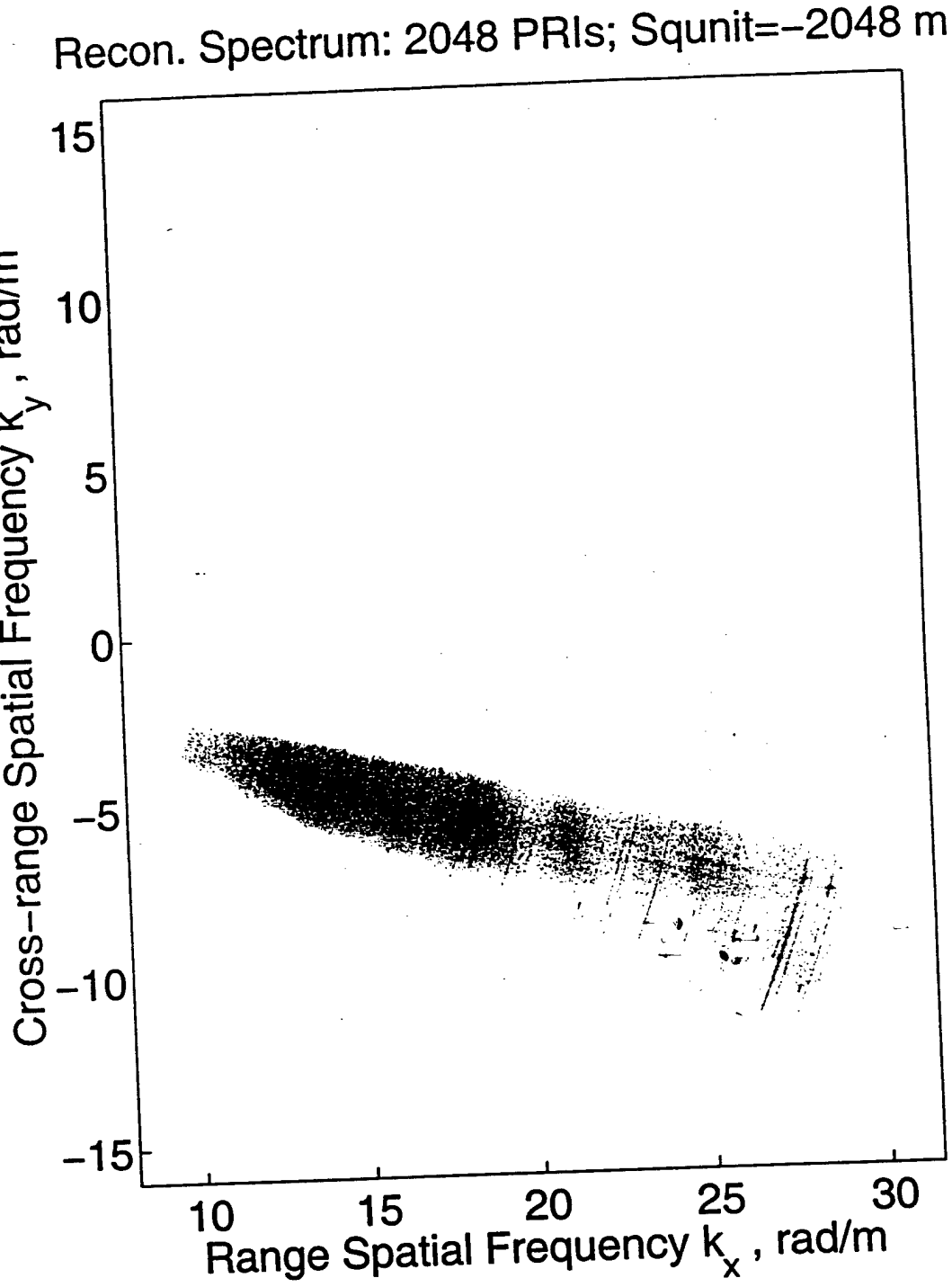
Recon. Spectrum: 2048 PRIs; Squnit=-2048 m
15
10
5
0
-5
-10
-15
Cross-range Spatial Frequency k_y , rad/m
10
15
20
25
30
Range Spatial Frequency k_x , rad/m

Figure 1a

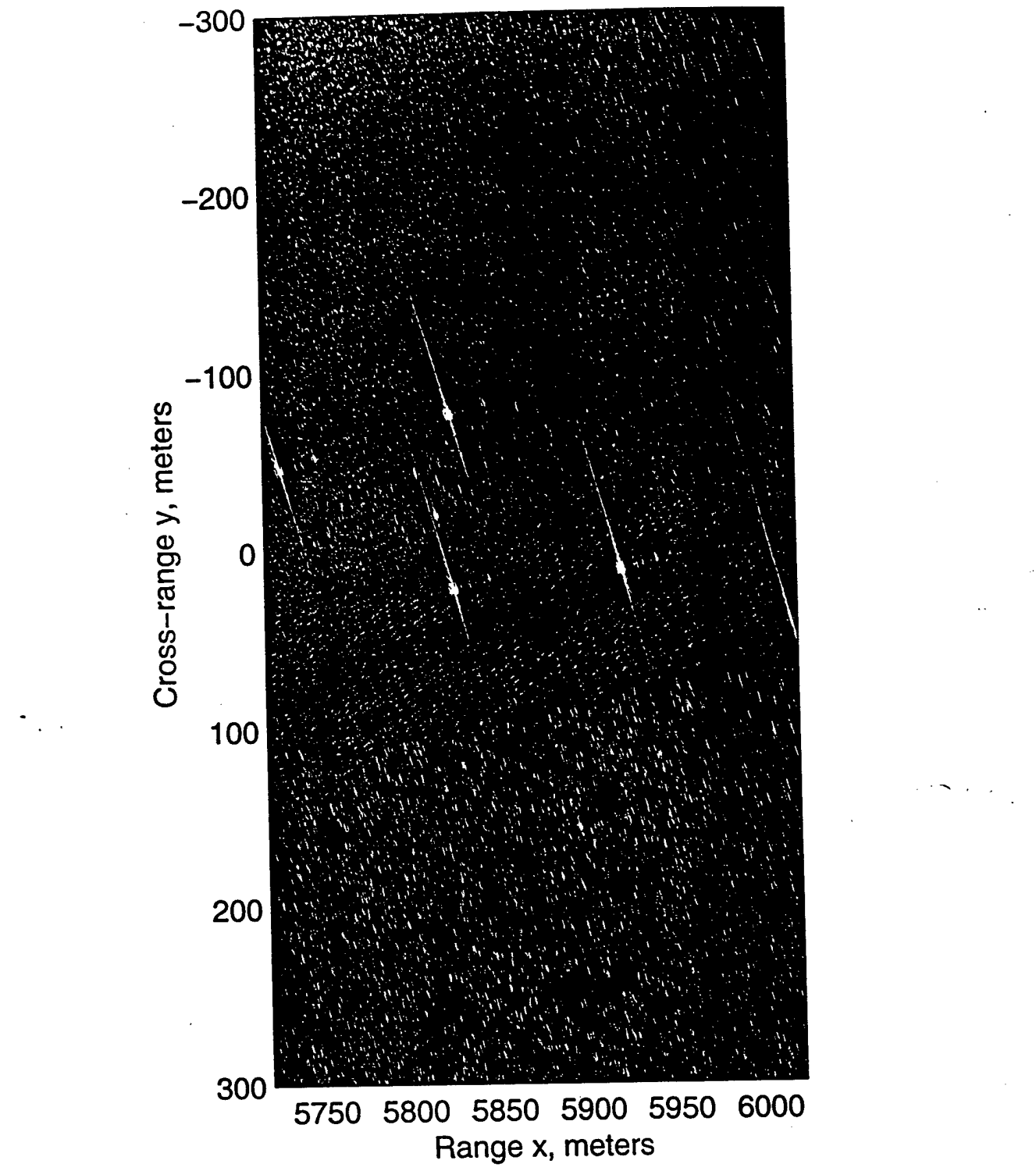
Wavefront SAR Reconstruction: P-3 Data; 2048 Pulses; Squint Y_r= -2048 m
-300
-200
-100
0
100
200
300
Cross-range y, meters
5750
5800
5850
5900
5950
6000
Range x, meters

Figure 1b

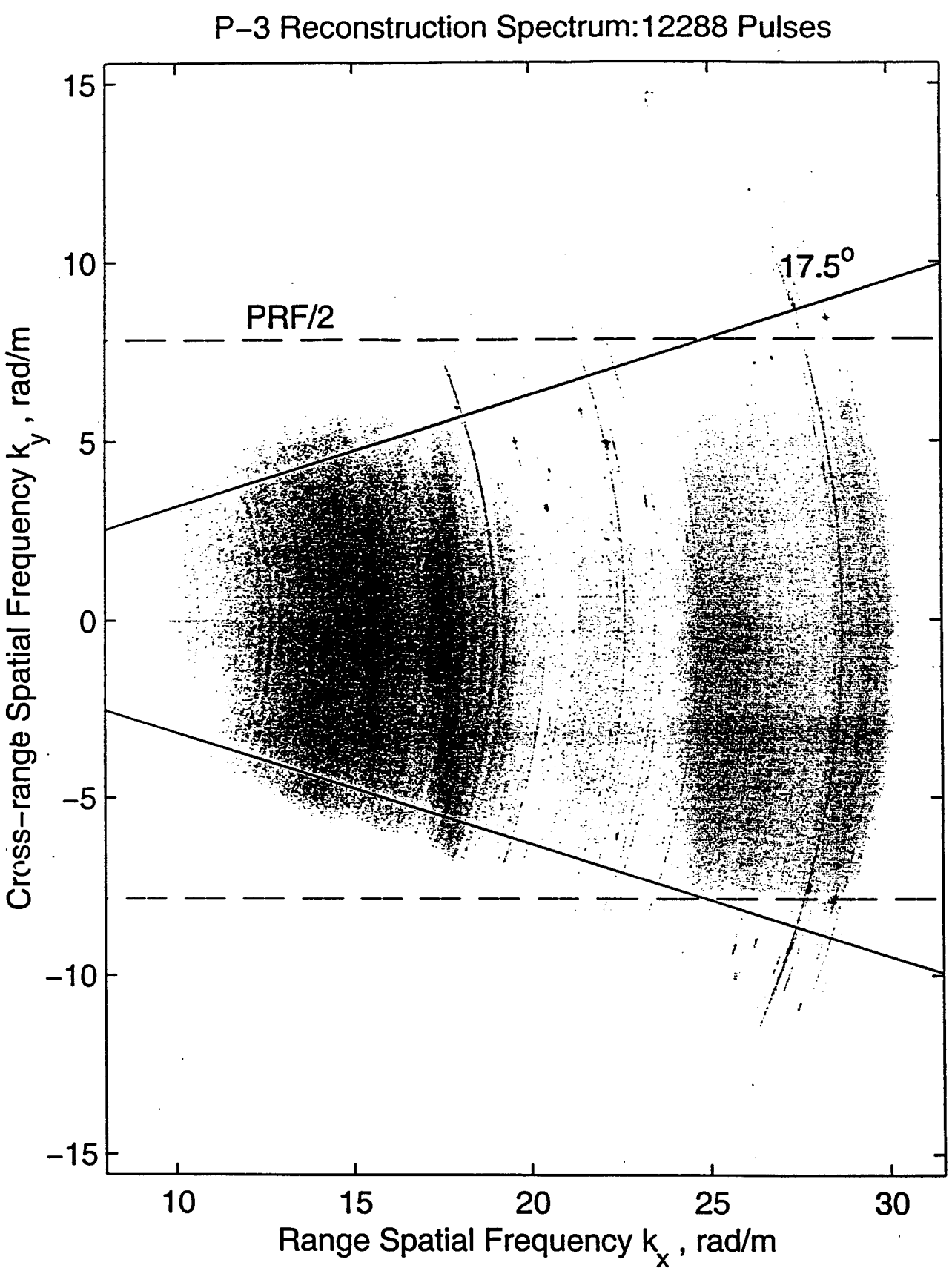
P–3 Reconstruction Spectrum:12288 Pulses
15
10
5
0
−5
−10
−15
17.5°
PRF/2
Cross–range Spatial Frequency k_y , rad/m
10
15
20
25
30
Range Spatial Frequency k_x , rad/m

Figure 2

(a)

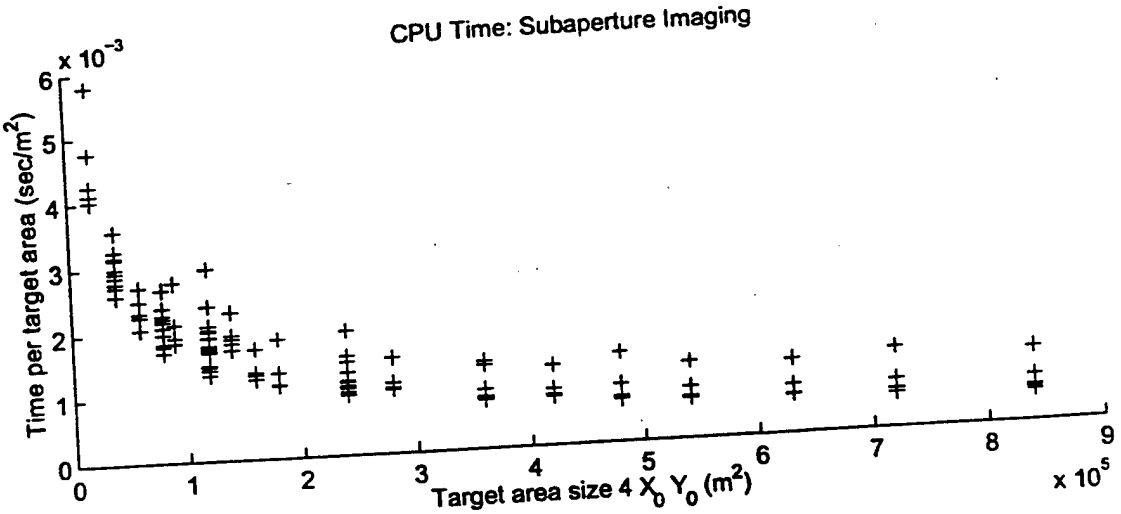
CPU Time: Subaperture Imaging
x 10^-3
Time per target area (sec/m^2)
Target area size 4 X0 Y0 (m^2)
x 10^5

(b)

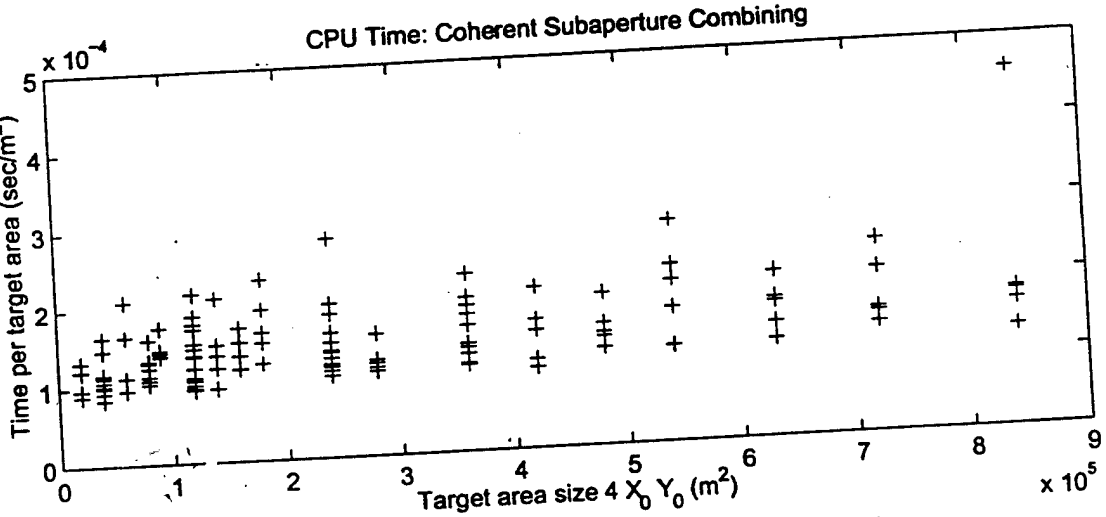
CPU Time: Coherent Subaperture Combining
x 10^-4
Time per target area (sec/m^2)
Target area size 4 X0 Y0 (m^2)
x 10^5

(c)

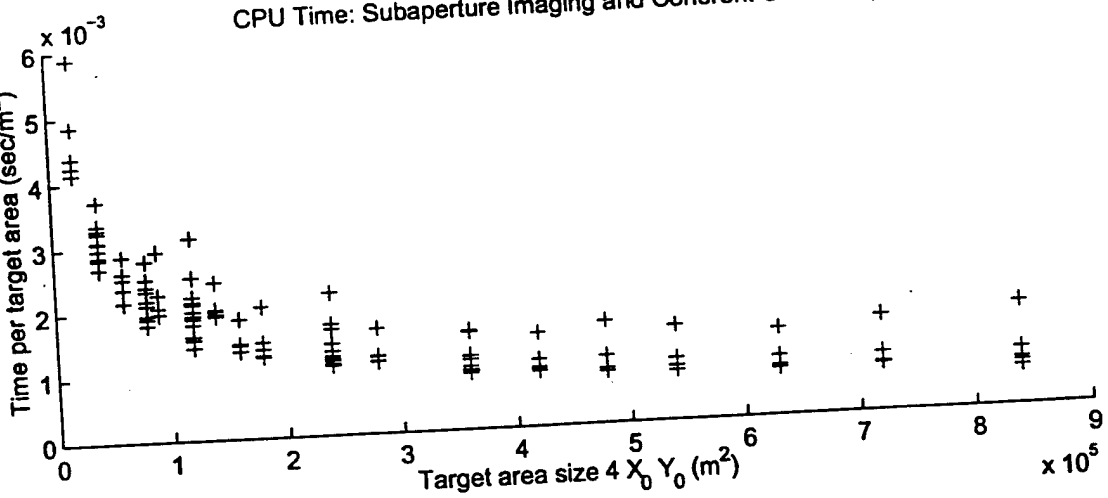
CPU Time: Subaperture Imaging and Coherent Combining
x 10^-3
Time per target area (sec/m^2)
Target area size 4 X0 Y0 (m^2)
x 10^5

Figure 3

SAR Wavefront Reconstruction Using Motion Compensated Phase History (Polar Format) Data and DPCA-Based GMTI

Mehrdad Soumekh
Department of Electrical Engineering, 201 Bell Hall
State University of New York at Buffalo
Amherst, New York 14260
Email: msoum@eng.buffalo.edu

Steve Worrell, Edward Zelnio and Brett Keaffaber
United States Air Force Research Laboratory/SNAS
2010 5th Street
WPAFB, OH, 45433

ABSTRACT

This paper address the problem of processing an X-band SAR database that was originally intended for processing via a polar format imaging algorithm. In our approach, we use the approximation-free SAR wavefront reconstruction. For this, the measured and motion compensated phase history (polar format) data are processed in a multi-dimensional digital signal processing algorithm that yields alias-free slow-time samples. The resultant database is used for wavefront image formation. The X-band SAR system also provides a two channel along-track monopulse database. The alias-free monopulse SAR data are used in a coherent signal subspace algorithm for Ground Moving Target Indication (GMTI). Results are provided.

Keywords: Synthetc Aperture Radar, Wavefront Reconstruction, Monopulse SAR, GMTI

1. INTRODUCTION

With the advent of powerful digital signal processing algorithms, both multidimensional signal analysis and reconstruction in imaging systems may now be formulated via more concrete theoretical principles. This is particularly true in SAR imaging. In the past decade, a new SAR imaging method, known as the SAR wavefront reconstruction, has been introduced that provides high-resolution and accurate coherent target information. Meanwhile, in the past thirty years an extensive theoretical and practical knowledge base has been shaped by the SAR polar format imaging that is based on approximations; some of these concepts are either incorrect or not applicable when viewed in the framework of the modern high-resolution SAR wavefront reconstruction.

A prominent example is encountered in X band spotlight SAR systems with a relatively large, e.g., 30-degree look angle. Based on the polar format processing, it is sufficient to acquire about 30,000 slow-time samples for this SAR system. However, based on the SAR wavefront reconstruction, the user should acquire and process more than 150,000 slow-time and/or cross-range samples for alias-free imaging. [1] Yet, the current operational SAR systems that acquire data based on the assumptions of the polar format

The work of Mehrdad Soumekh was supported by the Office of Naval Research under grants N00014-96-1-0586 and N00014-97-1-0966, and the Air Force Office Of Scientific Research under grants F49620-99-1-0140 and F49620-93-C-0063.

[1] If one utilizes digitally-spotlighted coherent subaperture imaging [S00], the slow-time samples are not required to be upsampled by a factor of five. However, the number of the cross-range samples for the full resolution image still is about 150,000.

processing, provide a motion compensated phase history (MCPH) data that contains only 30,000 slow-time samples.

In this case, the challenge for the user is to develop a method for converting the MCPH SAR data to alias-free SAR data, and form high-resolution images from the resultant database via the SAR wavefront reconstruction algorithm. This paper is concerned with developing such an algorithm, and implementing it for an operational spotlight SAR system. The application of the method in constructing a statistic that can be used as a ground moving target indicator (GMTI) in a DPCA-based spotlight SAR system is shown.

2. WAVEFRONT RECOSNTRUCTION USING MCPH DATA

A. Conversion of MCPH Data into Phase History Data

Let $s(\omega, u)$ be the measured spotlight SAR signal (phase history data) in the fast-time frequency ω domain and the synthetic aperture u domain. Suppose the spotlighted target area is identified via

$$x \in [X_c - X_0, X_c + X_0] \quad \text{and} \quad y \in [Y_c - Y_0, Y_c + Y_0],$$

where (X_c, Y_c) are the squint range and cross-range coordinates of the center of the target scene, and $2X_0$ and $2Y_0$ are the size of the spotlighted area in the range and cross-range domains, respectively.

The MCPH SAR data are samples of the slow-time compressed SAR signal, that is,

$$s_c(\omega, u) = s(\omega, u)\ \exp\left[j2k\ \sqrt{X_c^2 - (Y_c - u)^2}\right].$$

Thus, the phase history SAR data. that are samples of the SAR signal $s(\omega, u)$, can be recovered from the MCPH data via

$$s(\omega, u) = s_c(\omega, u)\ \exp\left[-j2k\ \sqrt{X_c^2 - (Y_c - u)^2}\right].$$

The main point that a user should keep in mind is that the slow-time sample spacing for the MCPH data (polar format processing) is

$$\Delta_u \leq \frac{R_c\ \lambda_{\min}}{4Y_0},$$

which is higher than the slow-time sample spacing of the SAR signal. Moreover, due to the imperfections in the analogly-spotlighted beam pattern (that is, the side lobes of the radar radiation pattern), there is some leakage from the targets that fall outside the desired (spotlighted) target area (that is, $x \in [X_c - X_0, X_c + X_0]$ and $y \in [Y_c - Y_0, Y_c + Y_0]$); these would introduce further slow-time Doppler aliasing in the desired SAR phase history data.

B. Digital Spotlighting and PRF Upsampling

Both of the above-mentioned slow-time Doppler aliasing-related problems can be surmounted via the digital spotlighting and PRF upsampling in [S99]. For this purpose, suppose the length of the subaperture is $2L$; that is, $u \in [-L, L]$, where u is the synthetic aperture domain. Let the coordinates of the center point of the target area with respect to the center point of the synthetic aperture (that is, $u = 0$) be (X_c, Y_c). The user is interested in imaging an area in the spatial domain that is specified via $x \in [X_c - X_0, X_c + X_0]$ and $y \in [Y_c - Y_0, Y_c + Y_0]$, with respect to the center of the aperture, that is, $u = 0$. Our task is to develop a multi-dimensional digital signal processing method to *extract* the SAR signature of the above-mentioned target area from the spotlight/stripmap measurements, a process that we refer to as *digital spotlighting*.

This can be achieved via the following steps. The reference SAR signal is defined via

$$s_0(u,\omega) = \exp\left[-j2k\ \sqrt{X_c^2 + (Y_c - u)^2} + j2k\ R_c\right];$$

the addition of the phase term $2k\ R_c$ to the reference signal ensures that the reference fast-time point T_c is unchanged. The digital spotlight filter in the (t, k_u) domain is defined via $W_d(t, k_u) = 1$ for

$$|\frac{c\ t}{2}\cos(\phi + \theta_c) - X_c| < X_0 \quad \text{and} \quad |\frac{c\ t}{2}\sin(\phi + \theta_c) - Y_c| < Y_0;$$

and zero, otherwise. Polar format processed reconstruction with the digital spotlight filter is

$$f_d(t, k_u) = W_d(t, k_u)\ \mathcal{F}_{(\omega,u)}\Big[\ s_c(\omega, u)\ \Big].$$

Then, the digital-spotlighted slow-time compressed SAR signal in the (ω, k_u) domain is obtained by

$$S_{cd}(\omega, k_u) = \mathcal{F}_{(t)}\Big[\ f_d(t, k_u)\ \Big].$$

To upsample the SAR data in the synthetic aperture u domain (that is. sample spacing conversion from Δ_{uc} to Δ_u), an appropriate number of zeros should be added to the samples of $S_{cd}(\omega, k_u)$ in the slow-time Doppler k_u domain S99, Chapter 2]. The Nyquist sampling rate for the slow-time domain which is the smallest of [S99]

$$\Delta_u \leq \frac{\lambda_{\min}}{2\ (\sin\theta_{\max} - \theta_{\min})} \quad \text{and} \quad \Delta_u \leq \Big[\ \frac{2\sin\theta_{\max}}{\lambda_{\min}} - \frac{2\sin\theta_{\min}}{\lambda_{\max}}\ \Big]^{-1}.$$

where $\lambda_{\min}$ and $\lambda_{\max}$ are, respectively, the smallest and largest wavelengths in the radar signal. and

$$\theta_{\min} = \arctan\left(\frac{Y_c - L - Y_0}{X_c}\right)$$

$$\theta_{\max} = \arctan\left(\frac{Y_c + L + Y_0}{X_c}\right)$$

are the smallest and largest aspect angles of the target area (a positive Y_c is assumed).

After the zero-padding in the k_u domain, the digital-spotlighted slow-time compressed signal in the (ω, u) domain is formed via

$$s_{cd}(\omega, u) = \mathcal{F}^{(-1)}_{(k_u)}\Big[\ S_{cd}(\omega, k_u)\ \Big].$$

Finally, the digital-spotlighted SAR signal in the (ω, u) domain is constructed from the following slow-time decompression (mixing with the reference SAR signal):

$$s_d(\omega, u) = s_{cd}(\omega, u)\ s_0(u, \omega).$$

C. Results

Figure 1a shows the polar format processed image using an X-band spotlight SAR database (called DDB data); the imaged area is about 380 m in range by 380 m in cross-range, and the dynamic range used to display the image is from -60 dB to -15 dB. Figure 1b is the imaged that is formed via the wavefront

reconstruction for approximately the same target area; the dynamic range used to display this image is also from -60 dB to -15 dB. The polar format image in Figure 1a exhibits shifting and smearing degradations at the edges of the 380 m by 380 m target area. In fact, the polar format processed image begins to show shift and smearing degradations for cross-range values that are about 80 meters away from the scene center. Note that for the same dynamic range of -60 dB to -15 dB, the polar format processed image shows stronger background clutter. The reason for this is that the strongest reflector in the scene is at the range/cross-range of $(x, y) \approx (0, -160)$ m that is *smeared* and shifted due to being relatively far from the scene center.

It is interesting to note that the quality (resolution) of the polar format processed image at the center of the target area [that is, $(x, y) \approx (X_c, Y_c)$] is also worse than the resolution obtained via the wavefront reconstruction algorithm in this region. (This should not have happened; the two methods should be equally good in the center of the target area.) We believe that the polar format processor is implemented with a filter that suppresses some of the streaking and smearing effects of the plane wave approximation at the edges of the formed image. Unfortunately, this filter also worsens the resolution of (contaminates) the polar format SAR image at the center of the target area.

Using the wavefront reconstruction processing for the X-band DDB data, we are able to form the image in Figure 1c that is 500 m in range and 1200 m in cross-range; the dynamic range used to display the image in Figure 1c is from -75 dB to -30 dB. We should mentioned that the target (spot) size of 1200 m in cross-range is beyond the anticipated 3 dB beamwidth of the radar antenna. In fact, the limiting factor for our processing (in the cross-range domain) is the PRF of the radar system.

3. PROCESSING OF UNCALIBRATED MONOPULSE SAR IMAGES FOR GMTI

A. GMTI Using Along-Track Monopulse SAR

Along track monopulse SAR imaging system utilizes two radars for its data collection. One radar is used as a transmitter as well as a monostatic receiver. The other radar is used only as a bistatic receiver. In [3], we documented a signal processing algorithm of the two monostatic and bistatic databases of the along track monopulse SAR system to obtain two *coherently* identical SAR images of the stationary targets in the scene. While the stationary targets appear the same in the monostatic and bistatic SAR images, however, the same is not true for moving targets.

This fact is the basis for developing a statistic, which we refer to as the difference image, for moving target detection. If we denote the monostatic SAR image by $f_m(x, y)$ and the bistatic image by $f_b(x, y)$, the difference image for moving target detection is defined via the following:

$$f_d(x, y) = f_b(x, y) - f_m(x, y).$$

The basic idea here is that the two sets of images that are formed in a monopulse SAR system, that is, $f_m(x, y)$ and $f_b(x, y)$, have a slight slow-time difference. In this case, the difference of the two monopulse images should yield information for GMTI (since the stationary targets do not vary in the slow-time). However, due to miscalibration between the two radars of the monopulse SAR system, a better model to relate the monopulse SAR images of a *stationary* target area is

$$f_b(x, y) = f_m(x, y) \ ** \ h(x, y),$$

where $**$ denotes two-dimensional convolution in the spatial domain, and $h(x, y)$ is an *unknown* (miscalibration) impulse response. Hence, one has to perform a *blind* calibration of the two images. A method

for this using a two-dimensional adaptive filtering and its implementation via a signal subspace processing method are described in [S99, Chapter 8].

B. Signal Subspace Processing

Adaptive filtering methods have been suggested to solve the above problem in one-dimensional cases. To apply these adaptive filtering methods in the two-dimensional problems, consider the discrete measured data in the (x_i, y_j) domain. The impulse response $h(x, y)$ is modeled by a finite two-dimensional discrete filter h_{mn}; the size of the filter, call it (N_x, N_y), is chosen by the user based on a priori information. In the following discussion, we choose both N_x and N_y to be odd integers, and $(n_x, n_y) = (N_x/2 - .5, N_y/2 - .5)$. Then, the above continuous model is rewritten in the following discrete form

$$f_b(x_i, y_j) = \sum_{m=-n_x}^{n_x} \sum_{n=-n_y}^{n_y} h_{mn}\, f_m(x_i - m\Delta_x, y_j - n\Delta_y) + f_e(x_i, y_j),$$

where (Δ_x, Δ_y) represent the sensor sample spacing in the (x, y) domain. In the adaptive filtering approach, a solution for the impulse response h_{mn} from the knowledge of $f_m(x_i, y_j)$ and $f_b(x_i, y_j)$, call it $\hat{h}_{mn}$, is obtained via minimizing the error function

$$\sum_i \sum_j \mid f_b(x_i, y_j) - \sum_{m=-n_x}^{n_x} \sum_{n=-n_y}^{n_y} \hat{h}_{mn}\, f_m(x_i - m\Delta_x, y_j - n\Delta_y) \mid^2.$$

The resultant solution is used to estimate $f_b(x_i, y_j)$ via

$$\hat{f}_b(x_i, y_j) \equiv \sum_{m=-n_x}^{n_x} \sum_{n=-n_y}^{n_y} \hat{h}_{mn}\, f_m(x_i - m\Delta_x, y_j - n\Delta_y).$$

The statistic used for detecting the foregin object is constructed from the following:

$$\hat{f}_d(x_i, y_j) \equiv f_b(x_i, y_j) - \hat{f}_b(x_i, y_j).$$

In the one-dimensional problems, the solution for $\hat{h}_m$ is formed via computing the inverse of a large covariance matrix, a recursive LMS (gradient descent adaptive) algorithm. These methods may be utilized in the two-dimensional problems via, e.g., *reshaping* the two-dimensional arrays into one-dimensional arrays. This, however, requires processing very large matrices, especially for the covariance matrix and the reshaped discrete filter.

The signal $\hat{f}_b(x_i, y_j)$ is the projection of $f_b(x_i, y_j)$ into the linear subspace which is defined by $f_m(x_i, y_j)$ and $N - 1$, where $N = N_x N_y$, of its shifted versions; i.e., $\Psi \equiv [\ f_m(x_i - m\Delta_x, y_j - n\Delta_y);\ m = -n_x, \ldots, n_x,\ n = -n_y, \ldots, n_y\ ]$. Thus, it is sufficient to identify the signal subspace Ψ. and then obtain the projection of $f_b(x_i, y_j)$ into this signal subspace to construct $\hat{f}_b(x_i, y_j)$. Let $\psi_\ell(x_i, y_j)$. $\ell = 1, 2, \ldots, N$, be a set of orthogonal basis functions which spans the linear signal subspace of Ψ; i.e., $\Psi = [\ \psi_\ell(x_i, y_j);\ \ell = 1.2, \ldots, N\ ]$, where

$$< \psi_\ell, \psi_k > \equiv \sum_i \sum_j \psi_\ell(x_i, y_j) \psi_k^*(x_i, y_j) = \begin{cases} 1, & \text{for } \ell = k; \\ 0, & \text{otherwise.} \end{cases}$$

To generate this signal subspace, one can use Gram-Schmidt, modified Gram-Schmidt, Householder or Givens orthogonalization procedure. The size of the signal subspace, i.e., N, depends on the user's a priori knowledge of the number of the nonzero coefficients in the discrete model of the impulse response $h(x,y)$. For instance, if the discrete $h(x,y)$ contains (N_x, N_y) non-zero pixels, then we should select $N = N_x N_y$. In practice, the exact value of $N_x N_y$ is not known. In this case, an estimate should be used based on the maximum anticipated degree of shift and calibration errors between the two sensors.

The projection of the $f_b(x_i, y_j)$ into the basis function $\psi_\ell(x_i, y_j)$, which is identified by the series coefficient a_ℓ $(\ell = 1, 2, \ldots, N)$, is found via the following:

$$a_\ell \equiv < \; f_b \; , \; \psi_\ell \; > = \sum_i \sum_j \; f_b(x_i, y_j) \; \psi_\ell^*(x_i, y_j)$$

The projection of $f_b(x_i, y_j)$ into the signal subspace Ψ is

$$\hat{f}_b(x_i, y_j) \equiv \sum_{\ell=1}^{N} \; a_\ell \; \psi_\ell(x_i, y_j).$$

The signal subspace difference image, i.e., the statistic for detecting the foreign object is constructed via (6b) $\hat{f}_d(x_i, y_j) \equiv f_b(x_i, y_j) - \hat{f}_b(x_i, y_j)$. Note that both the adaptive filtering method and the signal subspace projection of seek the same *minimum error energy* solution for the estimate of $f_b(x_i, y_j)$ in the linear subspace of $f_m(x_i, y_j)$ and its shifted versions.

C. Results

We now examine the GMTI results that are obtained using a DPCA (two antenna) database for the X band spotlight SAR system of Figure 1. Figure 2a shows the SAR reconstruction of a broadside target area that was obtained with the Channel 1 SAR data of the DPCA system. The Channel 2 reconstruction resembles the image in Figure 2a (not shown here). However, the coherent or noncoherent (magnitude) difference of the images of Channels 1 and 2 would not result in nulling of the stationary targets (not shown here). Figure 2b shows the block-based signal subspace difference image; for this, we use 20 pixels by 20 pixels blocks (approximately 5 m by 5 m), and a filter size of 5 pixels by 5 pixels. The vertical *streaks* in Figure 2b represent the signature of the moving targets. Note that some of these streaks (i.e., moving target signatures) are not visible in the original SAR reconstruction of Figure 2a.

Figure 3a shows the SAR reconstruction of an off-broadside target area that was obtained with the Channel 1 SAR data of the DPCA system: the target area is composed of a foliage region with moving targets in its surroundings. The Channel 2 reconstruction resembles the image in Figure 3a (not shown here). The coherent or noncoherent (magnitude) difference of the images of Channels 1 and 2 would not result in nulling of the foliage (not shown here). Figure 3b shows the block-based signal subspace difference image. The vertical *streaks* in Figure 3b represent the signature of the moving targets. Similar results for another target area that contains both stationary and moving targets are shown in Figures 4a-b.

References

[S99] M. Soumekh, *Synthetic Aperture Radar Signal Processing*, New York: Wiley, 1999.

[S00] M. Soumekh, G. Gunther, M. Linderman and R. Kohler, "Digitally-Spotlighted Subaperture SAR Image Formation Using High Performance Computing," *Proc. SPIE Aerosense*, Orlando, April 2000.

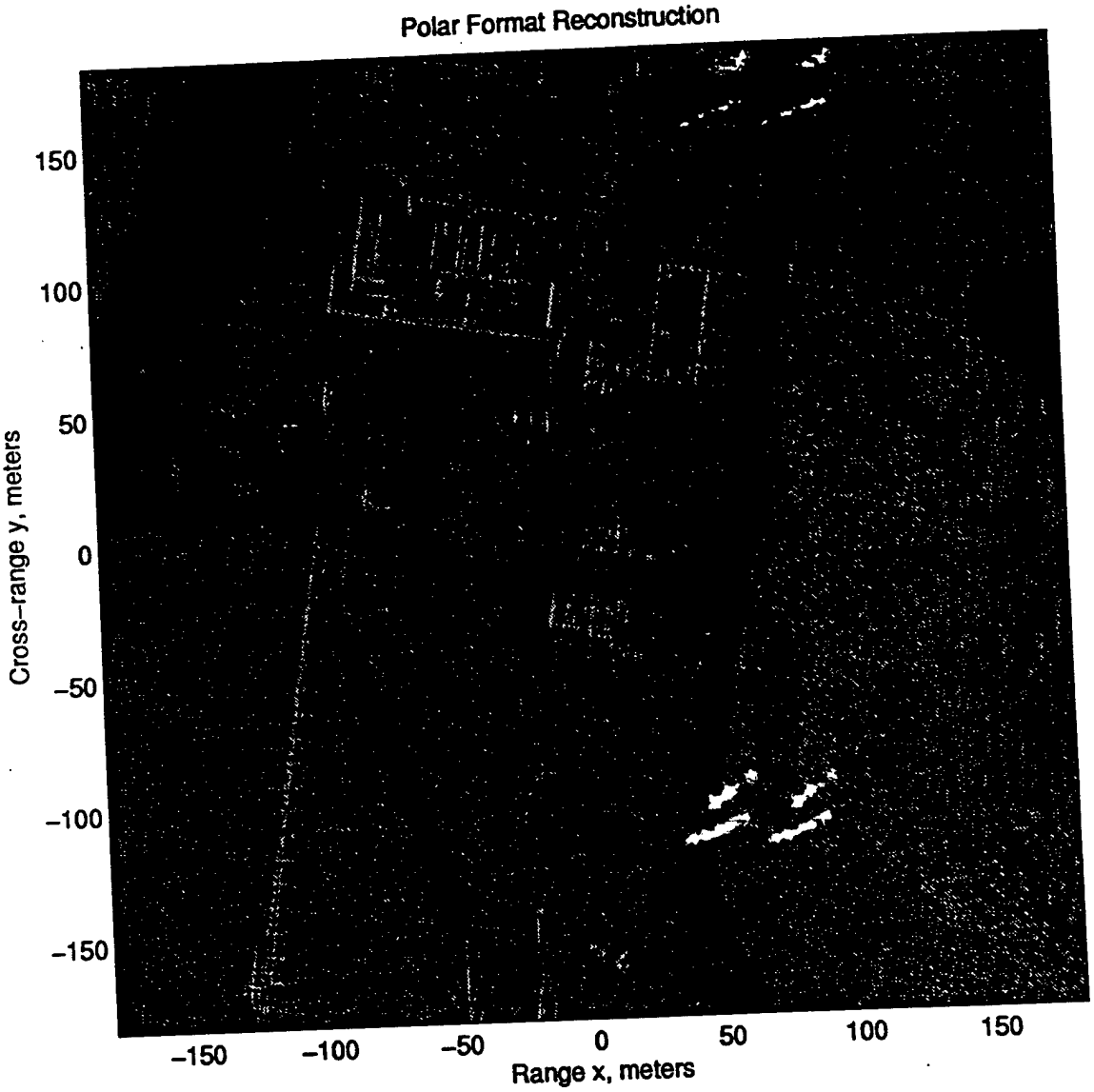

Figure 1a. Polar Format Reconstruction; dynamic range is -60 dB to -15 dB.

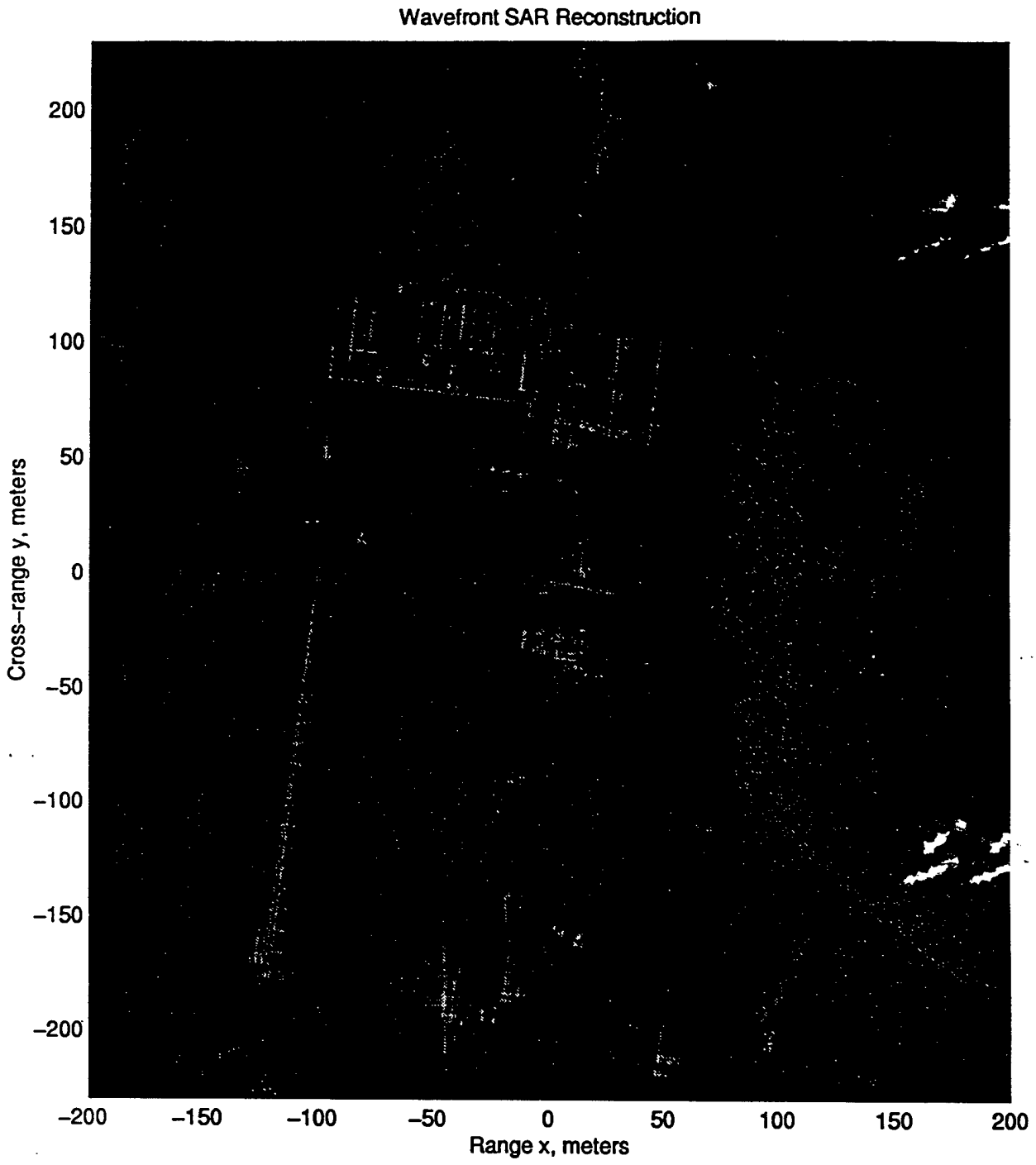

Figure 1b. Wavefront Reconstruction; dynamic range is -60 dB to -15 dB.

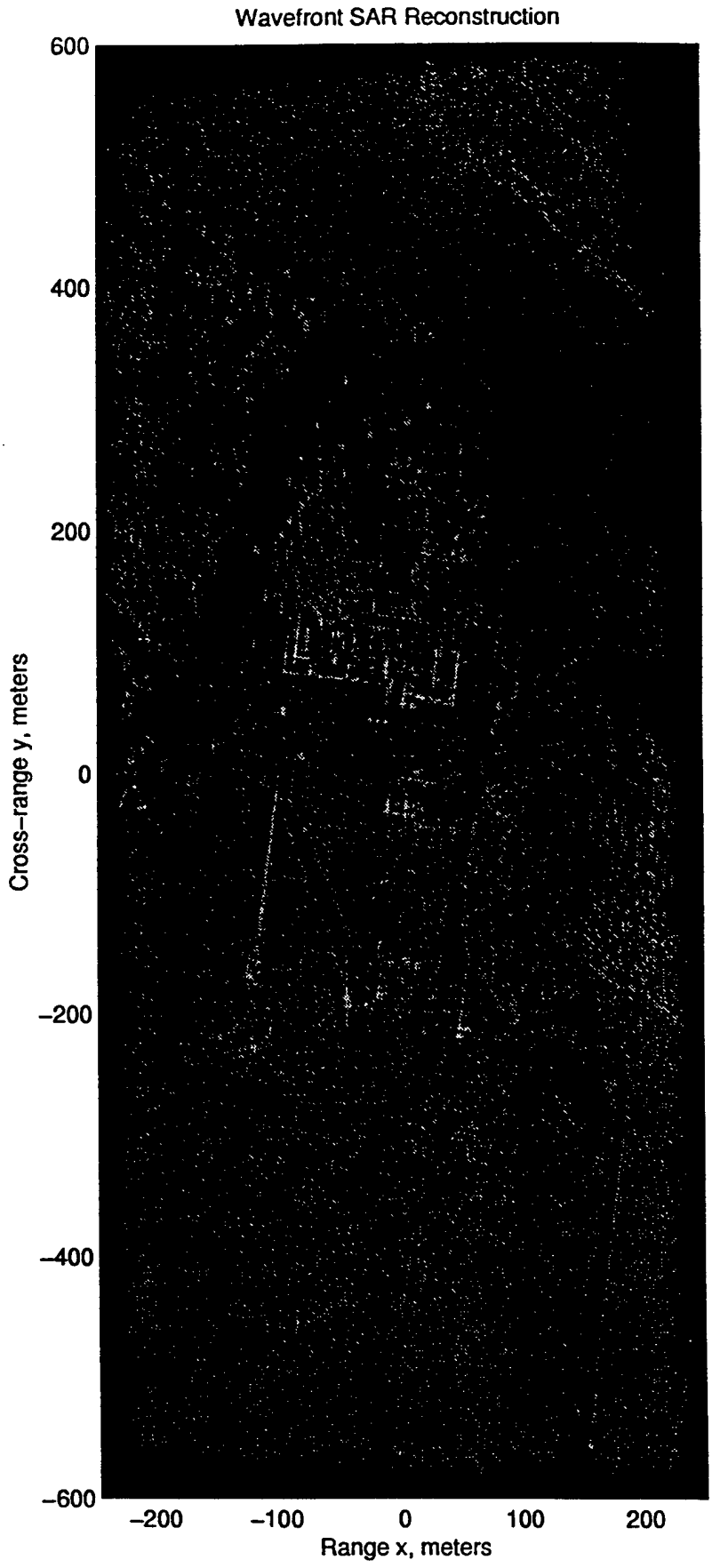

Figure 1c. Wavefront Reconstruction; dynamic range is -75 dB to -30 dB.

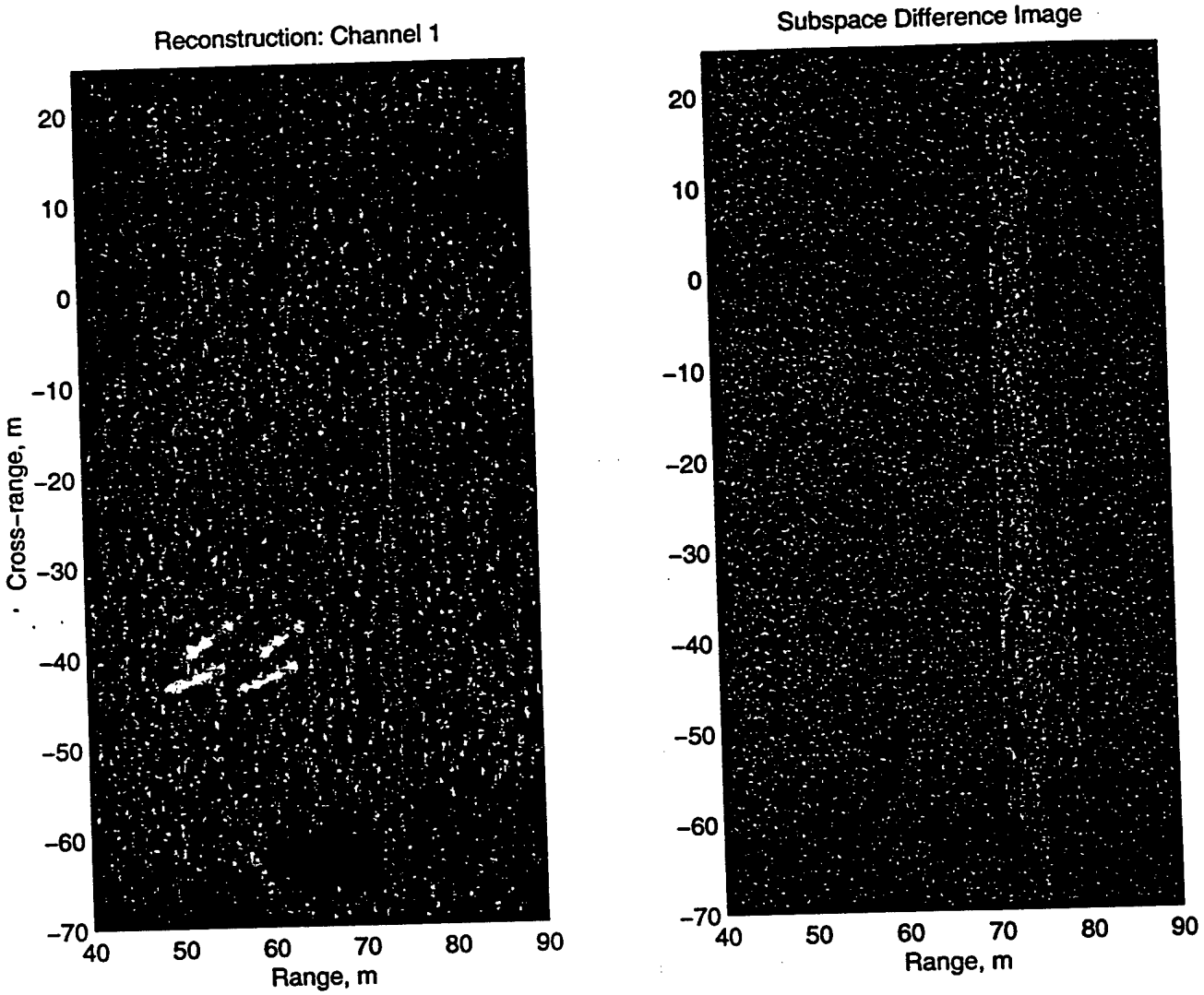
Reconstruction: Channel 1
Cross-range, m
20
10
0
-10
-20
-30
-40
-50
-60
-70
40
50
60
70
80
90
Range, m
(a)
Subspace Difference Image
20
10
0
-10
-20
-30
-40
-50
-60
-70
40
50
60
70
80
90
Range, m
(b)

Figure 2

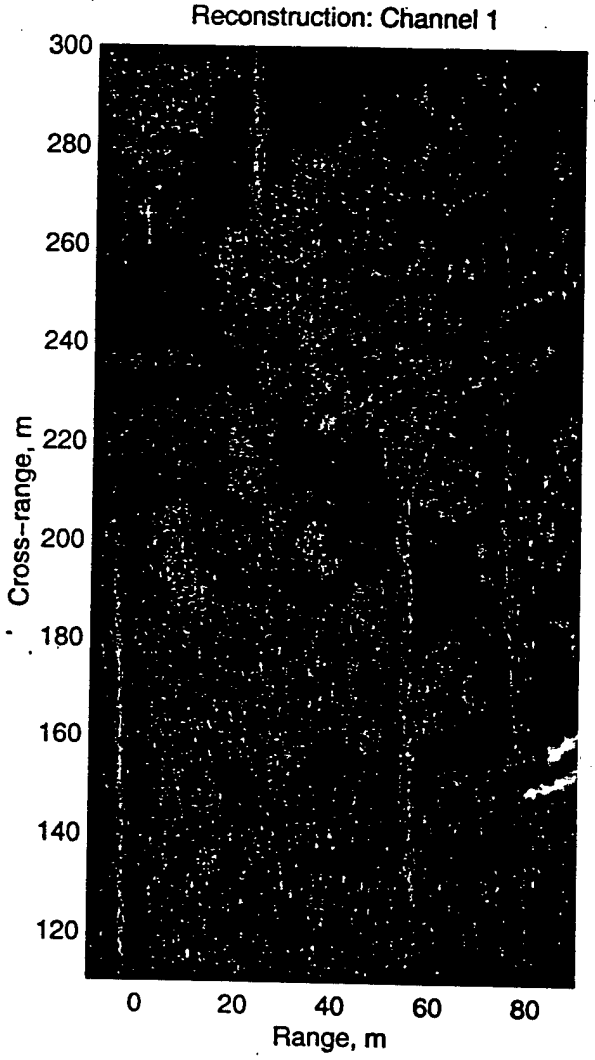
Reconstruction: Channel 1
300
280
260
240
220
200
180
160
140
120
Cross-range, m
0
20
40
60
80
Range, m

(a)

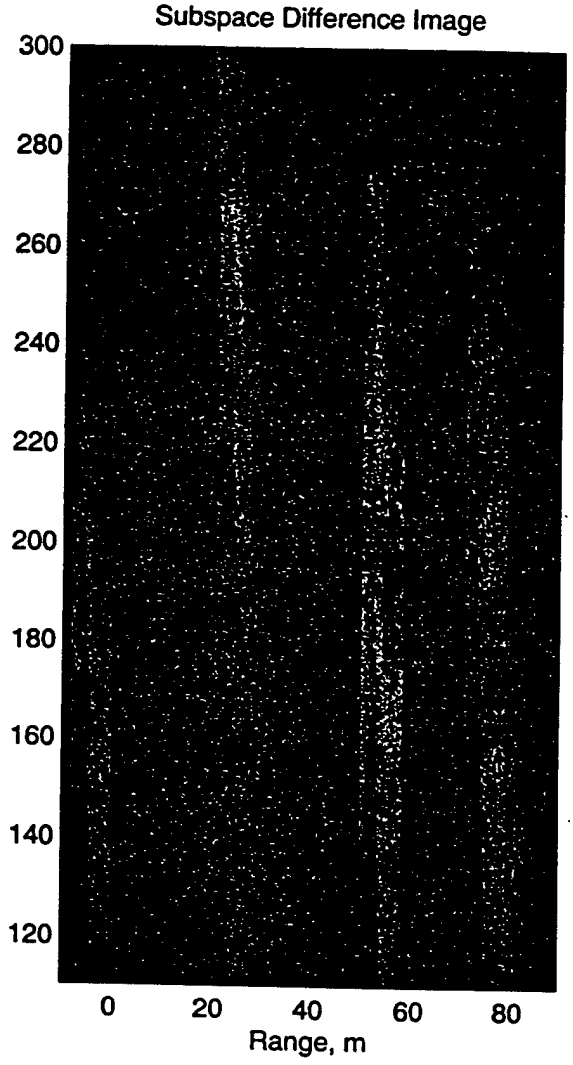
Subspace Difference Image
300
280
260
240
220
200
180
160
140
120
0
20
40
60
80
Range, m

(b)

Figure 3

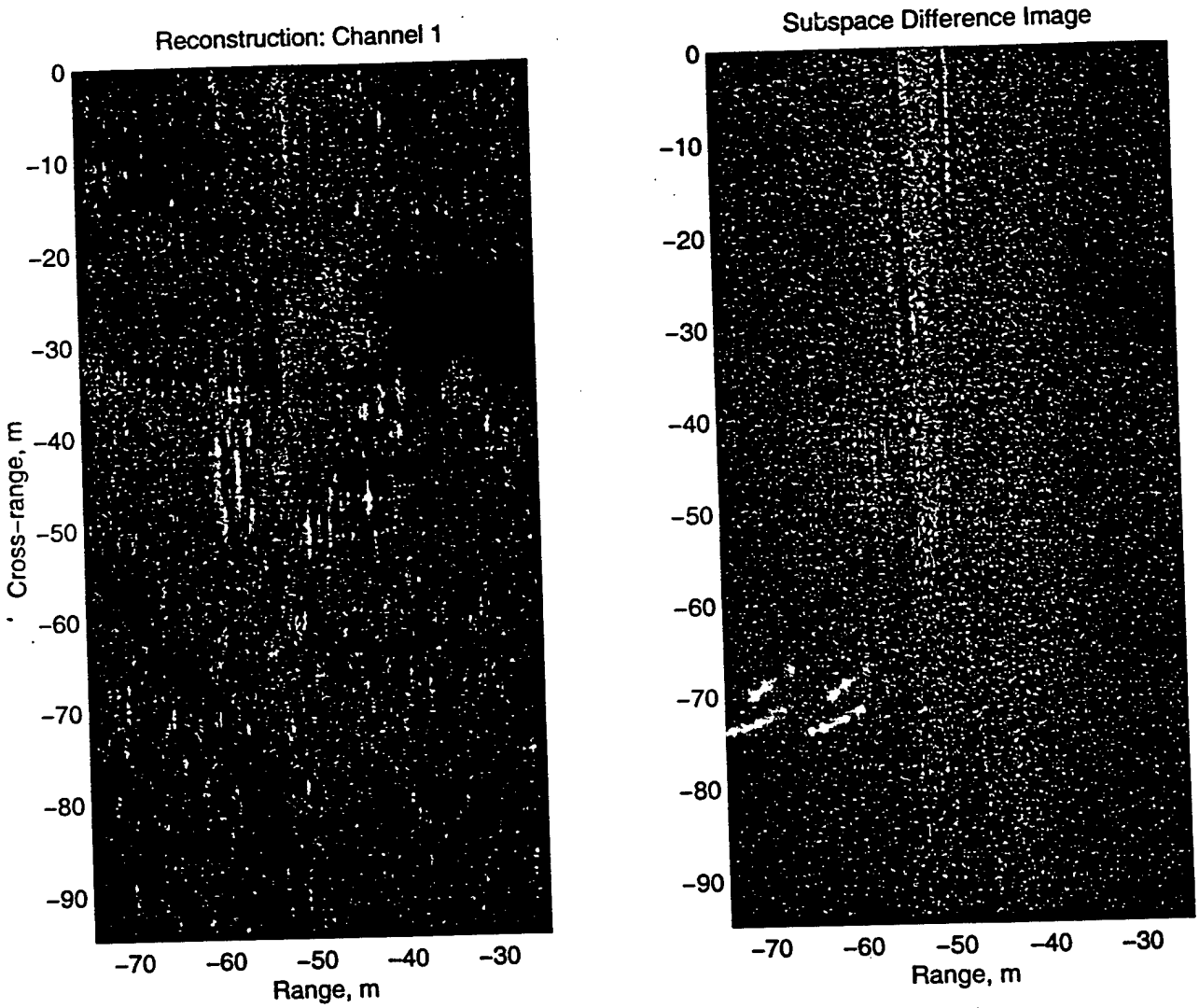
Reconstruction: Channel 1
0
-10
-20
-30
-40
-50
-60
-70
-80
-90
Cross-range, m
-70
-60
-50
-40
-30
Range, m
(a)
Subspace Difference Image
0
-10
-20
-30
-40
-50
-60
-70
-80
-90
-70
-60
-50
-40
-30
Range, m
(b)

Figure 4

Automatic Target Recognition in SAR Using Digitally-Spotlighted Phase History Data

Steve Worrell
United States Air Force Research Laboratory/SNAS
2010 5th Street
WPAFB, OH, 45433

Mehrdad Soumekh
Department of Electrical Engineering, 201 Bell Hall
State University of New York at Buffalo
Amherst, New York 14260
Email: msoum@eng.buffalo.edu

ABSTRACT

This paper is concerned with a representation of a target's complex Synthetic Aperture Radar signature that could be used for classification purposes. In this representation, the complex SAR signature of a desired target area (chip) as a function of the radar frequency and aspect angle (ω, ϕ) (i.e., the target area phase history data) are shown to directly map into the two-dimensional spectrum of the target's image via a nonlinear transformation; the same information base in the (ω, ϕ) domain is shown to be retrievable from the *digitally-spotlighted* complex SAR signature of the desired target region. For the classification problem (Automatic Target Recognition), the resultant complex SAR signature in the (ω, o) domain is compared with a finite and discrete set of *reference* complex SAR signatures via a process that we refer to as *signal subspace matched filtering.*

Keywords: Synthetc Aperture Radar, Automatic Target Recognition, Signal Subspace Matched Filtering

1. INTRODUCTION

This paper presents a new framework for Automatic Target Recognition (ATR) in Synthetic Aperture Radar (SAR) that is based on classification of the phase history data of individual targets. In the conventional SAR-ATR algorithms, the magnitude only or the complex SAR image of a target chip is analyzed to determine the target class. Depending on the relative coordinates of a target in the imaging scene and the flight path of the radar-carrying aircraft, the SAR image (chip) of a target possesses a spatial warping that should be incorporated and/or compensated for in the SAR image formation and the ATR algorithm. Furthermore, the formed SAR images exhibit certain (slant plane) parametric variations and even aliasing errors and erroneous shifts that depend on the type of the SAR imaging algorithm used and the individual who developed it.

For the success of a SAR-ATR algorithm, the spatial warping and slant plane parameters of the SAR imaging algorithm should be available to the user. However, often some or all of the above variations and parameters of the formed SAR image are unknown to the SAR-ATR user. These ambiguities, in conjunction with possible aliasing and erroneous shifts in the formed image, result in unknown geometric

The work of Mehrdad Soumekh was supported by the Office of Naval Research under grants N00014-96-1-0586 and N00014-97-1-0966, and the Air Force Office Of Scientific Research under grants F49620-99-1-0140 and F49620-93-C-0063.

distortions and errors in the reconstructed SAR image that have adverse effects on the performance of the SAR-ATR algorithms.

In this presentation, we provide a two-stage SAR-ATR algorithm that is not sensitive to the above-mentioned problems. In the proposed approach, the SAR-ATR user applies a relatively *fast* CFAR detection algorithm with a high probability of false alarm as well as a high probability of detection to identify the coordinates of suspected targets in a SAR imaging scene. Next, the coordinates (not the entire chip) of each suspected target is passed to what we refer to as the ***digital-spotlighting*** algorithm that extracts the SAR phase history data of a neighborhood within the input coordinates. We will also show that the SAR phase history data may also be formed by the inverse two-dimensional Fourier transform of the desired complex chip that is followed by a *nonlinear* mapping of the two-dimensional spatial frequency domain.

The resultant database is the complex SAR signature (phase history) of the chip area at the desired coordinates that carries information on the variations of the target's complex radar signature with respect to the fast-time (radar) frequency and aspect angle. This database could be passed through a finite order parametric modeling algorithm. The output of this algorithm is compared with a set of pre-existing parametric models (for tanks, trucks, foliage, clutter, etc.) to identify the class of the target at the input coordinates where the original ATR algorithm detected a suspected target.

A special algorithm for the above-mentioned modeling and matching is introduced, an algorithm that we call *signal subspace matched filtering*. that possesses the following desirable features:

i. The signal subspace matching algorithm is not sensitive to the calibration errors of the SAR system (i.e., variations of the radar radiation pattern from one experiment to another). Such calibration errors, that could drastically alter the *phase* information of a target's SAR signature, are one of the major obstacles in exploiting the *complex* SAR signature of a target in the classification problems.

ii. The pre-existing or *reference* targets' SAR signatures are commonly measured or generated (e.g., via the X-patch algorithm) at a finite and discrete set of fast-time (radar) frequencies and aspect angles, i.e., (ω, ϕ). In this case, the measured (extracted) SAR signature of a test target in the (ω, ϕ) domain may not correspond to the available discrete reference targets' SAR signatures; in this case, the test and its corresponding reference SAR signatures would not show ideal *registration*. The proposed signal subspace matching algorithm is not sensitive to this type of misregistration.

Our analysis begins with the characterization of a target SAR signature as a function of the radar frequency and aspect angle (Section 2). This is followed by identification of this signature in the two-dimensional spectral domain of the formed target image (Section 3). Finally, the signal subspace matched filtering method is outlined in Section 4.

2. TRANSMIT-RECEIVE MODE RADAR-TARGET RADIATION PATTERN AND ATR USING DIGITALLY-SPOTLIGHTED PHASE HISTORY DATA

The type as well as shape of a target determines its interaction with the radar illumination. For instance, the characteristics of the SAR signature of a man-made metallic cylinder is quite different from those of a tree with the same size. *This difference is a key feature which can be used to discriminate a man-made structure from foliage.*

Why not use shape information to distinguish targets in SAR images? Due to the radar wave resonance in cavities, surface waves, and the like, for metallic targets, the SAR image of these targets does not resemble

their optical image. Thus, *shape* (magnitude) information in a SAR image might not be a reliable source for target detection and identification. However, a target *coherent* SAR radiation pattern or coherent SAR image contains distinct features which could be used for target detection and identification.

We now present a study to quantify the coherent SAR signature of targets. A target exhibits an *amplitude pattern*, which contains *phase* as well as *magnitude*, when illuminated by a radar system such as SAR. *A target amplitude pattern varies with the radar fast-time frequency and aspect angle.* For a radar located at $(0, u)$ and a target located at (x_n, y_n), we denote the target amplitude pattern with $a_n(\omega, x_n, y_n - u)$. Note that

$$\arctan\left(\frac{y_n - u}{x_n}\right)$$

is the target aspect angle with respect to the radar broadside.

The coherent SAR signature of the n-th target is its contribution in the total echoed signal from the target scene. When the radar is located at $(0, u)$ and fast-time frequency ω, the coherent SAR signature of the n-th target, that is, the *transmit-receive mode radar-target radiation pattern* or *SAR radiation pattern* for the n-th target can be expressed via the following:

$$h_n(\omega, x_n, y_n - u) = \underbrace{h_T(\omega, x_n, y_n - u)}_{\text{Radar-to-Target}} \; \underbrace{a_n(\omega, x_n, y_n - u)}_{\text{Target}} \; \underbrace{h_R(\omega, x_n, y_n - u)}_{\text{Target-to-Radar}};$$

in the above model. $h_T(\cdot)$ is the radar transmit mode radiation pattern, $h_R(\cdot)$ is the radar receive mode radiation pattern [S99].

Substituting for $h_T(\cdot)$ and $h_R(\cdot)$ in terms of their amplitude patterns and spherical PM signal in the n-th target SAR radiation pattern, we obtain

$$\begin{aligned} h_n(\omega, x_n, y_n - u) = {} & a_T(\omega, x_n, y_n - u) \; \exp\left[-jk\sqrt{x_n^2 + (y_n - u)^2}\,\right] \\ & \times \; a_n(\omega, x_n, y_n - u) \\ & \times \; a_R(\omega, x_n, y_n - u) \; \exp\left[-jk\sqrt{x_n^2 + (y_n - u)^2}\,\right] \end{aligned}$$

A block diagram representation of the generation of the SAR radiation pattern for the n-th target is shown in Figure 1.

Using the expression for the radar transmit-receive mode radiation pattern

$$\begin{aligned} h(\omega, x, y) &= h_T(\omega, x, y)\, h_R(\omega, x, y) \\ &= a(\omega, x, y) \; \exp(-j2k\sqrt{x^2 + y^2}) \end{aligned}$$

where

$$a(\omega, x, y) = a_T(\omega, x, y)\, a_R(\omega, x, y),$$

in the SAR radiation pattern of the n-th target, one obtains

$$\begin{aligned} h_n(\omega, x_n, y_n - u) == {} & a_n(\omega, x_n, y_n - u) \;\; h(\omega, x_n, y_n - u) \\ = {} & \underbrace{a_n(\omega, x_n, y_n - u)\, a(\omega, x_n, y_n - u)}_{\text{Amplitude Pattern}} \; \underbrace{\exp\left[-j2k\sqrt{x_n^2 + (y_n - u)^2}\,\right]}_{\text{Spherical PM Signal}} \end{aligned}$$

We showed earlier that the radar amplitude pattern $a(\omega, x_n, y_n - u)$ is related to the physical size and to the type of the radar used. The magnitude of the radar amplitude pattern $|a(\omega, x_n, y_n - u)|$ dictates

its *power* at the coordinates of the n-th target at the fast-time frequency ω. The spherical PM signal $\exp\left[-j2k\sqrt{x_n^2+(y_n-u)^2}\right]$ is the round trip phase delay of the echo from the n-th target at the fast-time frequency ω.

Once a target area (chip) is identified by a CFAR algorithm as a potential man-made target, the user could extract the target amplitude pattern $a_n(\cdot)$ via the *digital spotlight* algorithm [S99, Chapters 5-6]; the size and location of the digitally-spotlighted area are dictated by the coordinates and the size of the chip. This approach is summarized in Figure 2.

3. REPRESENTATION IN SLOW-TIME ANGULAR DOPPLER DOMAIN AND SPECTRAL DOMAIN-BASED ATR

Based on the properties of AM-PM signals [S99, Chapter 2], we have the following slow-time Fourier transform for the transmit-receive mode radar-target radiation pattern:

$$\mathcal{F}_{(u)}\left[h_n(\omega, x_n, y_n-u)\right] = A(\omega,k_u)\ A_n(\omega,k_u)\ \exp\left(-j\sqrt{4k^2-k_u^2}\ x_n - jk_u\ y_n\right),$$

where the target and radar amplitude patterns in the u and k_u domains are related via the following:

$$a_n(\omega,x_n,y_n-u) = A_n\left[2k\sin\theta_n(u),\omega\right]$$
$$a(\omega,x_n,y_n-u) = A\left[2k\sin\theta_n(u),\omega\right],$$

and

$$\theta_n(u) = \arctan\left(\frac{y_n-u}{x_n}\right)$$

is the n-th target *aspect angle* when the radar is located at $(0,u)$.

- *Reminder: The amplitude-functions $a(\cdot)$ [or $a_n(\cdot)$] and $A(\cdot)$ [or $A_n(\cdot)$] are* **scaled** *transformations of each other, and not Fourier transform pairs.*

The *angular* slow-time Doppler domain [S99] is defined via

$$\phi = \arcsin\left(\frac{k_u}{2k}\right),$$

or

$$k_u = 2k\ \sin\phi.$$

Recall that the slow-time domain AM signal $a_n(\omega,x_n,y_n-u)$ and the slow-time Doppler domain AM signal $A_n(\omega,k_u)$ are related via the following scale transformation:

$$A_n(\omega,k_u) = \frac{1}{r_n^2}\ a_n(\omega,x_n,y_n-u),$$

where the mapping is defined via

$$k_u = 2k\ \sin\theta_n(u).$$

Thus, the scale mapping of the AM signals in the angular slow-time Doppler domain is

$$\phi = \theta_n(u).$$

The above indicates that the AM signature of a target in the aspect angle $\theta_n(u)$ domain, that is, $a_n(\cdot)$, directly maps into the slow-time angular ϕ domain to form the AM component of $S_n(\omega, k_u)$.

This phenomenon is demonstrated in Figure 3a-b. Figure 3a shows the aspect angles of the n-th target at $u = -L$, $u = 0$, $u = L$, and the Closest Point of Approach (CPA) $u = y_n$ which are, respectively, $\theta_n(-L)$, $\theta_n(0)$, $\theta_n(L)$, and $\theta_n(y_n) = 0$. Figure 3b shows the slow-time Doppler mapping of the AM component in the slow-time angular Doppler ϕ domain. For this purpose, the slow-time angular Doppler ϕ domain is shown as the *polar* angle domain of

$$k_x = \sqrt{4k^2 - k_u^2}$$
$$k_y = k_u$$

or

$$k_x = 2k \cos\phi$$
$$k_y = 2k \sin\phi$$

which are the range spatial frequency and cross-range spatial frequency domains, respectively; the above is called the SAR spatial frequency mapping [S99].

Next, we use the slow-time angular Doppler variable ϕ to redefine the slow-time Fourier transform of the AM-PM signal, that is,

$$S_n(\omega, k_u) = A_n(\omega, k_u) \exp\left(-j\sqrt{4k^2 - k_u^2}\, x_n - jk_u\, y_n\right).$$

via

$$S_n(\omega, 2k \sin\phi) = A_n(\omega, 2k \sin\phi) \exp\left(-j2k \cos\phi\, x_n - j2k \sin\phi\, y_n\right).$$

Also, we define the AM signal of the n-th target in the slow-time angular Doppler domain by

$$A_{pn}(\omega, \phi) = A_n(\omega, 2k \sin\phi).$$

Thus, we may rewrite the AM-PM signal in the angular slow-time Doppler domain by

$$S_n(\omega, 2k \sin\phi) = A_{pn}(\omega, \phi) \exp\left(-jk_x\, x_n - jk_y\, y_n\right).$$

The equivalence of the aspect angle $\theta_n(u)$ domain and the slow-time angular Doppler ϕ domain in the mapping of the AM signature of a target plays a key role in characterizing the target SAR image; this is crucial for target *recognition* or *detection* in SAR images. For this, suppose a CFAR algorithm identifies a target chip, call it $f_n(x, y)$, as a potential man-made structure. The user could form its two-dimensional spectral image $F_n(k_x, k_y)$ via a two-dimensional (discrete) Fourier transform. Finally, the target complex amplitude pattern is obtained via mapping $F_n(k_x, k_y)$ from the (k_x, k_Y) domain into $\omega, \phi)$ domain via the following nonlinear two-dimensional transformation (SAR *inverse* mapping):

$$\omega = \frac{c}{2}\sqrt{k_x^2 + k_y^2}$$
$$\phi = \arctan\left(\frac{k_y}{k_x}\right)$$

The resultant database if then used for classification; this procedure is outlined in Figure 4.

4. SIGNAL SUBSPACE MATCHED FILTERING

Next, we consider the problem of registration of the *reference* and *test* SAR signatures of a target. In practice, the user faces subtle phase and gain variations in the two *complex* SAR signatures. These subtle variations are due to the changes of the point spread function for the two SAR systems, and incremental changes in the relative orientation of the target with respect to the radar (small shift, scaling and rotation). These factors are outlined in the following.

i. The flight path and altitude of the radar-carrying aircraft may vary slightly in the reference run (or the simulated X-patch run) and the test run. This causes a relative scaling and rotation of targets in the two SAR signatures.

ii. The two radars exhibit calibration errors. This is discussed and modeled in [S99, Section 8.2].

iii. The two SAR data contain different residual motion errors (even after motion compensation). This results in a fast-time frequency and slow-time (aspect angle) dependent phase error.

iv. In the case of a simulated reference target signature (e.g., X-patch data), the reference target SAR signature is generated at a finite and discrete set of radar frequencies and aspect angles that may not correspond to the measured SAR signature of a test target.

We denote the (discrete) reference target signature by $A_{pn1}(\omega, \phi)$ and the (discrete) test target signature by $A_{pn2}(\omega, \phi)$. (Note that a simulated reference signature A_{pn1} is commonly available or generated for all aspect angle $\phi[-\pi, \pi)$: however, the test target signature A_{pn2} might be measured only within a few degrees of aspect angle.) Due to the above-mentioned calibration and misregistration errors, the two-dimensional matched-filtering (or correlation) of these two signatures, i.e.,

$$< A_{pn2}(\omega, \phi) , A_{pn1}(\omega, \phi) >,$$

would not result in ther ideal correlation results. However, the calibration and misregistration errors could be circumvented by the signal subspace projection of $A_{pn2}(\omega, \phi)$ into $A_{pn1}(\omega, \phi)$ [S99 ection 8.3]; this operation can be viewed as a two-dimensional *blind equalization* or *adaptive filtering*.

Let $\hat{A}_{pn2}(\omega, \phi)$ be the resultant subspace projection. The signal subspace matched filtering is defined to be the correlation of this subspace projection and the reference target signature; i.e..

$$< \hat{A}_{pn2}(\omega, \phi) , A_{pn1}(\omega, \phi) > .$$

References

[S99] M. Soumekh, *Synthetic Aperture Radar Signal Processing with MATLAB Algorithms*, New York: Wiley, 1999.

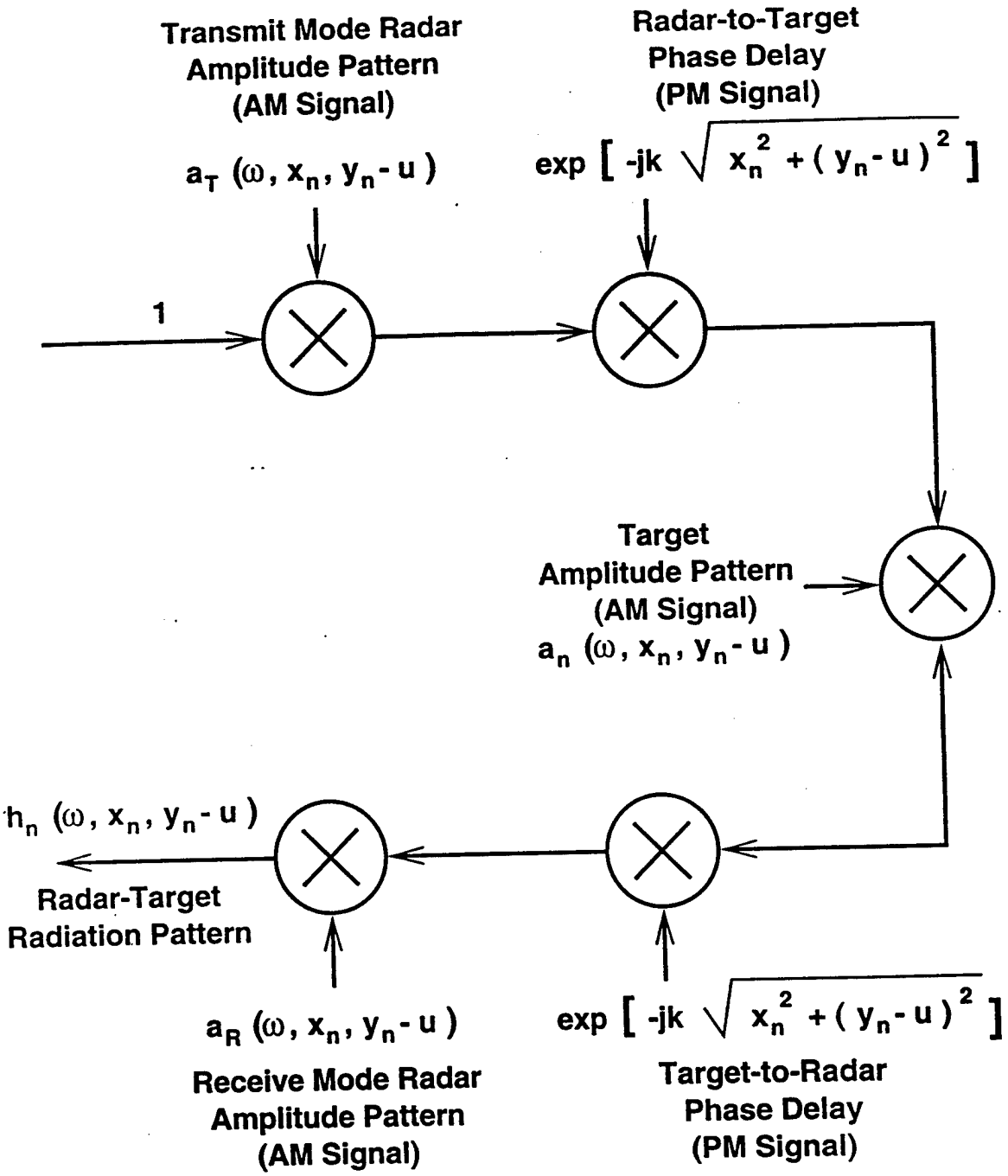

Block Diagram Representation of SAR Signal

Figure 1

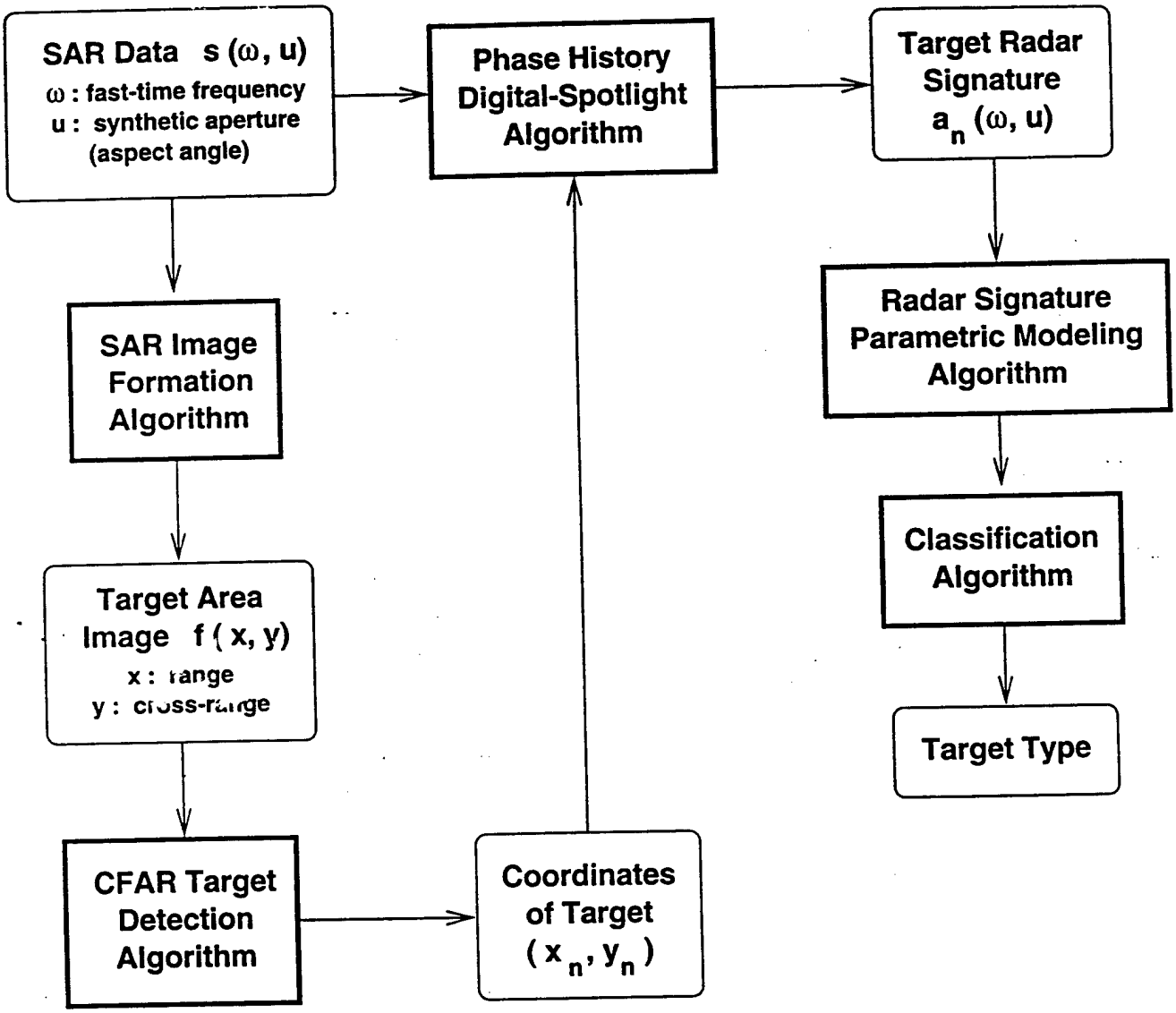
SAR Data s (ω, u)
ω : fast-time frequency
u : synthetic aperture (aspect angle)
Phase History Digital-Spotlight Algorithm
Target Radar Signature a_n (ω, u)
SAR Image Formation Algorithm
Radar Signature Parametric Modeling Algorithm
Classification Algorithm
Target Area Image f (x, y)
x : range
y : cross-range
Target Type
CFAR Target Detection Algorithm
Coordinates of Target (x_n, y_n)

Figure 2

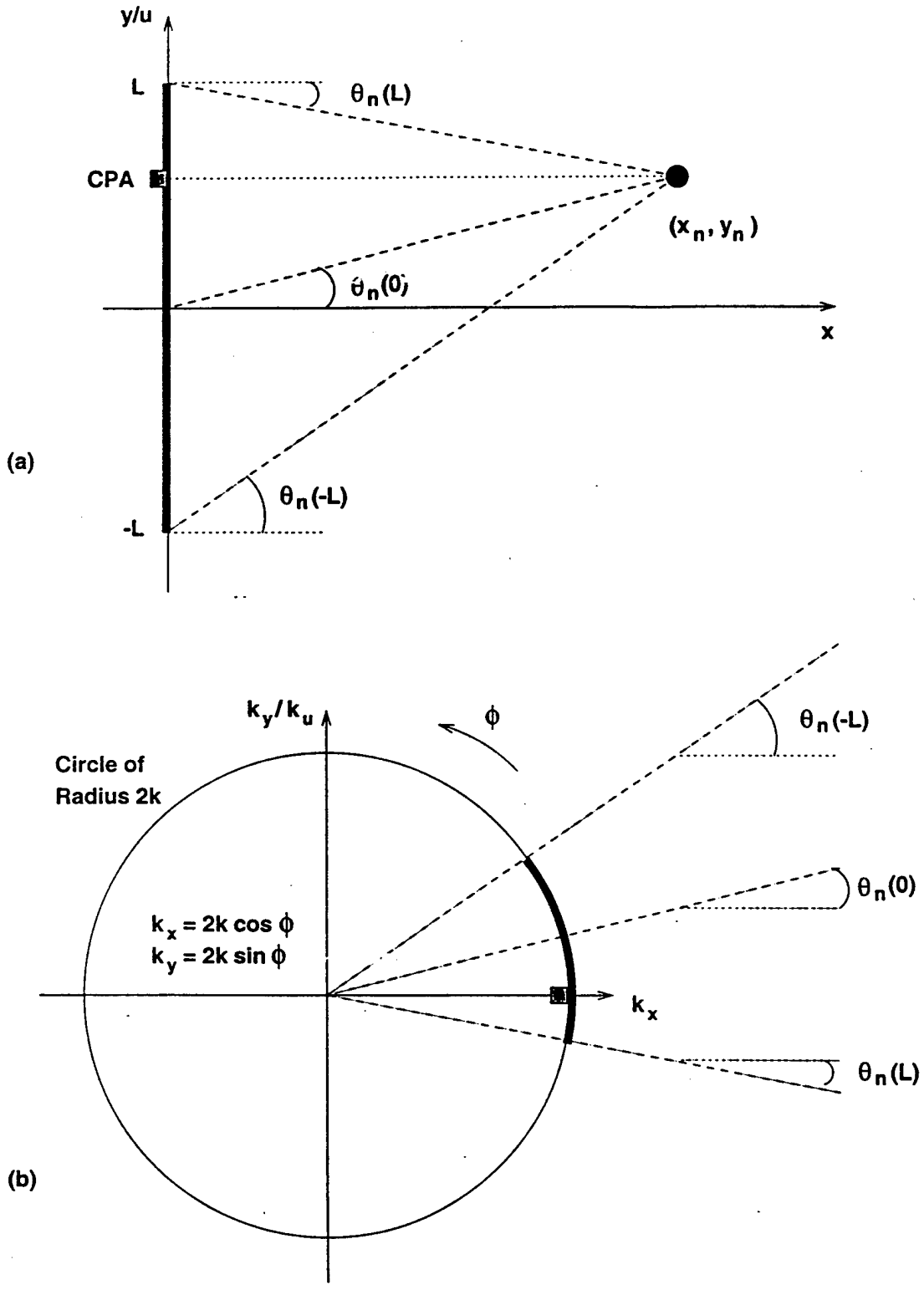

Mapping of Synthetic Aperture Data (at a Fixed Fast-time Frequency) into Target's Spectral Domain

Figure 3

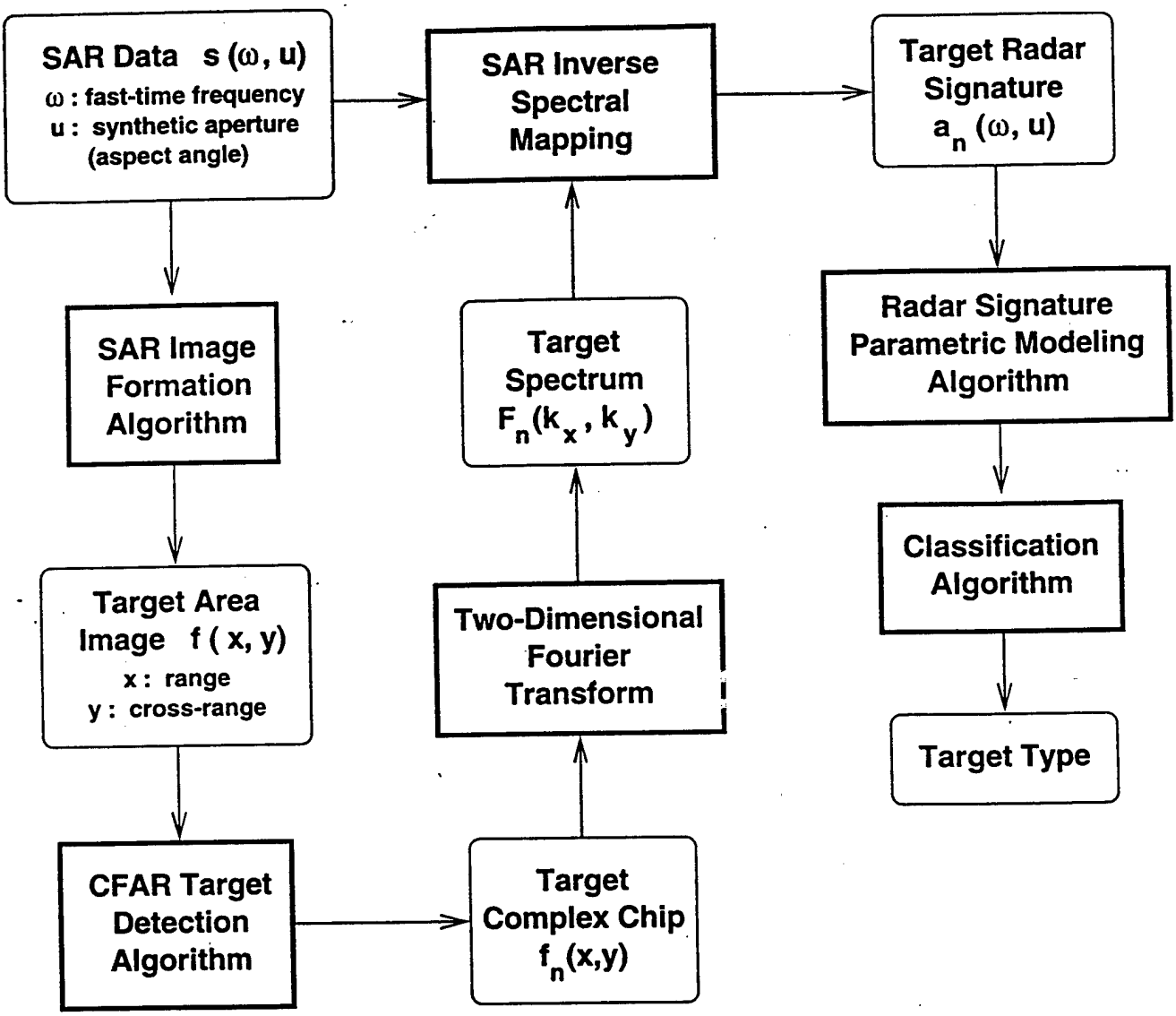
SAR Data s (ω, u)
ω : fast-time frequency
u : synthetic aperture (aspect angle)
SAR Inverse Spectral Mapping
Target Radar Signature a_n (ω, u)
SAR Image Formation Algorithm
Target Spectrum $F_n(k_x, k_y)$
Radar Signature Parametric Modeling Algorithm
Target Area Image f (x, y)
x : range
y : cross-range
Two-Dimensional Fourier Transform
Classification Algorithm
Target Type
CFAR Target Detection Algorithm
Target Complex Chip $f_n(x,y)$

Figure 4